designs

MDPI

Article

Design and Operational Assessment of a Railroad Track Robot for Railcar Undercarriage Condition Inspection

James Kasch and Mehdi Ahmadian *

Railway Technologies Laboratory (RTL), Center for Vehicle Systems and Safety (CVeSS), Virginia Polytechnic Institute and State University, Blacksburg, VA 24060, USA; jamesk18@vt.edu
* Correspondence: ahmadian@vt.edu

Abstract: The operational effectiveness of a railroad track robot that is designed for railcar undercarriage inspection is provided. Beyond describing the robot's design details and onboard imaging system, the paper analyzes the recorded video images and offers design improvements to increase their clarity. The robot is designed to be deployed trackside, traverse over the rails, and then maneuver in between the rails beneath a stopped train in a siding or a railyard. The under-carriage conditions are documented by onboard video cameras for automated or manual postprocessing. The intent is to inspect the components that are not visible to the conductor or train inspector during a walk-along inspection of a stationary train. An assessment of the existing design, followed by modification and validation, is presented. The results from a prototype unit developed by the Railway Technologies Laboratory at Virginia Tech (RTL) indicate that with proper positioning of off-the-shelf imaging systems such as cameras manufactured by GoPro® in San Mateo, CA, USA and appropriate lighting, it is possible to capture videos that are sufficiently clear for manual (by a railroad engineer), semi-automated, or fully automated (using Artificial Intelligence or Machine Learning methods) inspections of rolling stock undercarriages. Additionally, improvements to the control, mobility, and reliability of the system are documented, although reliability throughout operation and the ability to consistently climb out of the track bed remain points of future investigation.

Keywords: railcar; inspection; robotics; design modification; video image; safety; track robot

Citation: Kasch, J.; Ahmadian, M. Design and Operational Assessment of a Railroad Track Robot for Railcar Undercarriage Condition Inspection. *Designs* **2024**, *8*, 70. https://doi.org/10.3390/designs8040070

Academic Editors: Roveda Loris and Roberto Meattini

Received: 28 April 2024
Revised: 20 June 2024
Accepted: 1 July 2024
Published: 10 July 2024

1. Introduction

The 80 billion USD freight rail industry in the U.S. operates on nearly 225,000 km of track and supports the U.S. economy by providing more than 167,000 jobs and supplying the most efficient cargo land transport [1]. In the 2023 fiscal year, a total of 1947 train accidents were reported to the Federal Railroad Administration (FRA) in the U.S., of which 1299 were derailments [2]. Although these numbers have been reduced substantially from 20 years ago, when 2991 accidents, 2124 of which were derailments, occurred during the 2003 fiscal year, continued innovation is needed to maintain this trend, ensuring that the railroads remain safe, efficient, and competitive in the ever-adapting global market.

The developments in wayside train monitoring system (WTMS) technology in recent years have contributed to decreased accident rates. WTMSs are stationary systems installed trackside that perform autonomous inspections on in-motion rolling stock with various sensors providing advanced condition monitoring and defect detection. WTMSs have been in use since the 1930s and 1940s, when hot-box and dragging equipment detectors were first developed, and are still widely used to this day [3–5]. State-of-the-art WTMSs are now capable of detecting much more. Studies have now shown methods for utilizing strain gauge, accelerometer, acoustic, and thermal imaging data for the detection of wheel flats [6], wheel-rail impact forces [7,8], unbalanced loads [9], lateral and vertical wheel-rail contact forces [10], and defective bearings [11]. There are also WTMSs that utilize machine vision to monitor the rolling stock and detect defects [12–14]. Some of these systems

use an inspection pit to create thermal and video images of the railcar undercarriage, which are then analyzed offline for potential defects using image processing algorithms. Such systems, however, require track modifications and capital investments that can be substantial. Additionally, they are stationary, and their use is limited to the rail traffic at their specific track location.

Wayside imaging systems have also been shown to be able to identify and locate critical components on rolling stock, such as wheels, journal-bearing bolts, suspension springs, and others, using convolutional neural networks (CNNs) and other image processing models [15,16]. Expanding on these technologies, more recently, inspection portals have been installed on the Class I revenue service track that capture 360° images of rolling stock at speeds up to 140 km/h [17,18]. High-speed cameras and lighting systems are used to capture more than 1000 clear images per rail car. Some systems use artificial intelligence (AI) models to process the images for potential defects. These systems help railroads gather advanced condition monitoring data from their rolling stock. However, the 360° inspection portals described above are limited to in-motion inspections and are out of reach for all but the Class I railroads, with unit costs reportedly near 3 million USD [19].

Alongside the major advancements to WTMSs, inspection methods for stationary railcars have, conversely, remained nearly unchanged throughout the past decades. FRA regulations dictate that each railcar in an assembled train must be inspected before it is cleared to depart the railyard [20]. In these pre-departure inspections, carmen are responsible for inspecting the full length of the train, which at times can be over 3 km long [21]. Making this process more difficult, many critical components on a railcar (center sills, side sills, brake rigging, coupler pin plates, etc.) lie on the undercarriage in areas that are difficult, time-consuming, and hazardous to inspect manually [18]. Additionally, the time allotted for these inspections was from 3 to 4 min per car as a standard in the past; however, some current reports now state carmen are given only 60 s per car (a fact that has come under scrutiny after the widely covered derailment in East Palestine last year) [22]. A method for providing the carmen inspection data from the undercarriage could allow them to focus their inspection efforts on areas suspected of containing defects, thus increasing the effectiveness, efficiency, and safety of these inspections. Schlake et al. [23] conducted an analysis indicating that the railroad industry could save 35 million USD annually if WTMS data were used to target inspection efforts during intermediate stationary inspections. This study focused on using en route WTMS data for defect detection to aid in a later stationary inspection; however, providing this data via a mobile, cost-effective platform could bring advanced condition monitoring capabilities to every railyard for pre-departure and other stationary inspections.

Mobile inspection platforms have been developed and are used for undercarriage inspections of road vehicles. Schoenherr and Smuda [24] detail an undercarriage robot for the inspection of incoming vehicles at a military base. The device is designed to detect suspicious materials while keeping the operator out of harm's way. The device operates autonomously using a 3D laser rangefinder to construct a model of the undercarriage and compare it to a template of the vehicle's make and model before traversing to areas where the scans differ and providing inspectors with video footage of these locations. Commercial products, such as the HADES inspection robots developed by Techmatics NZ, provide similar capabilities, autonomously traversing beneath vehicles while providing operators with live imagery data from video, line scan, or thermal imaging cameras [25].

Mobile inspection platforms have been developed and are used today in the railway industry. Railway inspection robots are capable of monitoring rail and track health and identifying missing components [26]. Today, railway inspection robots are proven systems and are commercially available [27,28]. Most of these robots traverse on the rails, which eliminates the possibility of modifying these platforms for any form of rolling stock inspection. Daniyan et al. [29] detail the design and simulation of a rail inspection robot that traverses using a set of tracks; however, the construction and testing of the robot have not been actualized to the knowledge of the authors. A few mobile train inspection robots

currently exist or are in development. The ANYmal, an autonomous quadruped robot, has been used in partnership with Stadler Rail for the inspection of stationary rolling stock at service locations [30]. The ANYmal can traverse beside the train, gathering data from the side of the car and wheelsets. It can also inspect the undercarriage of the train using a recessed inspection pit or inspect the inside of the cabin; however, this system does not currently appear to be able to traverse beneath rolling stock in revenue service conditions where no recessed inspection pit is present.

Kiselev and Korkina [31] present the design of a tracked mobile robot to inspect the sides of railcars in a maintenance facility using various sensors, including video cameras, ultrasonic sensors, and eddy current detectors. This design is limited to the maintenance facility environment and does not appear to be able to inspect the undercarriage. Additionally, to the knowledge of the authors, the design's construction has not been actualized.

A few studies explore the possibilities of using autonomous robots for undercarriage inspection [32,33]. Imaging and 3D point cloud data are gathered from these robots for defect detection. However, nearly all these systems are only functional in the inspection pit environment, eliminating them from consideration for use in railyards and sidings.

Chiaradia et al. [34] present the development of an undercarriage inspection robot that traverses using wheels that run on the rail web and foot. The study based in Italy shows the robot can be installed between the rails of a revenue service track and can travel beneath rolling stock without interference. An operator remotely controls an articulated arm carrying a depth camera to investigate specific components during the inspection. This system, however, cannot capture the entire undercarriage in a single pass and currently requires manual control of the arm to reach each component of interest, which may become time-consuming and monotonous for the operator. As it uses the rail web for a running surface, it can also not be used in tracks where rail joints are present. Lastly, its need to be manually installed between the tracks requires time that the carmen could use for the inspection.

To help bridge this technological gap and bring WTMS-level condition monitoring to stationary inspections on a mobile, cost-effective platform, the Railway Technologies Laboratory at Virginia Tech (RTL) has developed the Track Crawler Robot (TCR) shown in Figure 1. The TCR is a mobile, remote-controlled track robot designed to be deployed trackside, climb unassisted over the track, traverse beneath railcars, perform a turn to operate in reverse direction, and continuously capture clear images of the full railcar undercarriage in a single pass. The images could be used by carmen to supplement their visual inspection or as a stand-alone means of inspection. These images could be integrated into a semi-automated or automated defect detection system utilizing machine learning (ML) or AI to process the images and autonomously notify carmen of areas in need of further inspection. Additionally, the video images can be stored to provide historical evidence of the condition of the rolling stock post-derailment or accident. A video has been included in the Supplementary Materials to show the TCR operating beneath a train as intended during real-world inspections.

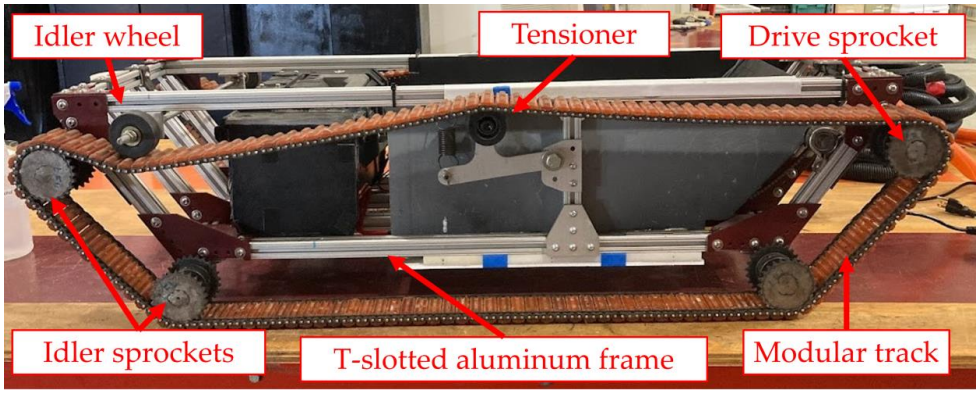

Figure 1. Existing design of the Track Crawler Robot (TCR).

1.1. Design Considerations

The TCR's key design specifications were informed by its intended operating conditions. Its height was limited to 330 mm (13 in.) to ensure clearance beneath all standard freight railcars. Its width was designed to be within 760 mm (30 in.) to allow clearance between the rails. The standard U.S. rail gage width is 1435 mm (56.5 in.). The length of the TCR was similarly constrained to be within 1220 mm (48 in.) to allow clearance for operating perpendicular to the rail direction, such as when climbing in and out of the track bed and when turning. A continuous track system was chosen for locomotion due to its simplicity, durability, and excellent traction. Its weight was limited to 45 kg (100 lbs.) to allow deployment by a team of two, typical for pre-departure inspections. Material costs were limited to 3000 USD, placing this technology in the price range of both Class I and short-line customers. The specific design details resulting from these technological limitations are presented in the following chapter.

1.2. Operational Challenges and Known Design Drawbacks

The operating conditions defined for this project raise a number of challenges. Molzon and Ahmadian [35] presented the initial development of the TCR and, in doing so, uncovered two design drawbacks requiring further investigation. In this paper, the design of the TCR was covered in detail, and preliminary tests were conducted focusing on the performance of the imaging system. This paper revealed that at speeds greater than 2.6 km/h, motion blur begins to obscure the contents of the images. Motion blur occurs when objects being imaged travel a noticeable distance while the camera's shutter is exposed. The camera captures the course of the object, leading to blur, which can greatly obscure any information in the image. The TCR will likely need to operate above this speed to maximize the efficiency of the inspection as required by the railroads. Additionally, the tests in the paper were performed on asphalt, a relatively smooth surface. The TCR must image clearly while operating on the track bed. The track bed comprises wooden ties and ballast, creating a varying and rough surface to traverse, Figure 2a. These conditions will introduce substantial vibrations into the system and will most likely heighten the effect of motion blur at a given operating speed. The paper also detailed the system's reliance on ambient light, as it was without any supplemental lighting system. Without a lighting system, the TCR will only have sufficient lighting to conduct inspections during the day, if at all, making it dependent on the ambient conditions when a robust solution is required.

(**a**) (**b**)

Figure 2. (**a**) The TCR operating on the track bed beneath a railcar; (**b**) A hopper railcar illustrating the low height of the gates above the track bed.

Another operational challenge is the field of view (FOV) required by the imaging system for full undercarriage inspection. Components are expected to be as low as 410 mm above the track bed in the case of hopper railcar gates, Figure 2b [36,37], and the TCR should be able to image low-lying components across the entire standard U.S. rail gauge of 1435 mm (56.5 in.) to cover the area between the rail wheels, which is most difficult for inspectors to view and contains many critical components as stated. This required FOV is very wide, spanning over 140° laterally from the existing camera mounting location, 160 mm above the track bed. The FOV was not explicitly investigated in the previous paper.

Control within the track bed is another operational concern. The TCR will be subject to disturbances throughout the inspection. At the same time, the TCR will pass partially or fully out of view when it traverses between the rail wheels or beneath low-lying components. Additionally, the TCR can only be viewed from the side while beneath the rolling stock, making it difficult to determine its heading and position within the rails while timely and precise steering inputs are required to maintain course and avoid collisions. The TCR was initially designed for line-of-sight control feedback, and no control loop existed around the control signal and the response of the TCR. Lastly, the track bed environment poses mobility and reliability challenges to the TCR. The TCR is rigidly supported by idler sprockets and has no suspension; therefore, the rough environment of the track bed could impose significant shock loads on the frame and damage components. The reliability of the system in these conditions is assessed, and modifications are conducted where necessary. Additionally, maneuvers such as rail climbing and turning via differential steering while in the track bed are necessary for the unassisted operation and are evaluated.

1.3. Contributions

This paper's main contribution is refining the TCR system to clearly image an entire railcar undercarriage in a single pass. This capability is unique to the TCR. To the knowledge of the authors, no other device can capture the entire undercarriage of a railcar in a single pass while in the railyard and siding environments. The study also presents a comprehensive assessment of the TCR's capabilities. The system's control methodology is enhanced by providing the operator with video feedback and integrating a control loop regulating the TCR's speed. The reliability of the TCR is enhanced through the informed redesign of a failure-prone drivetrain subsystem. These improvements are all validated through testing, and the results are presented. The results demonstrate a self-propelled railcar undercarriage inspection robot with unique capabilities that have not yet been shown in the literature. This paper brings robot-assisted inspections of stationary railcars one step closer to the market.

1.4. Redesign Methodologies

As noted, this paper documents the redesign and modification of the TCR system. The subsystems subject to redesign were identified through an assessment designed to mimic the various operational challenges expected during real-world inspections. Based on the nature of the subsystem needing improvement, varying redesign methods were applied. The redesign of mechanical subsystems was first informed by the unique requirements of the subsystem, e.g., a frame member must be relocated to increase the FOV of the imaging system. Secondly, engineering judgment was applied to create and refine concepts. Finally, calculations and simulations, including finite element analysis (FEA) and modal analysis, were conducted to validate the concepts. In the case of the lighting system, it was possible to quantify the degree to which the subsystem was inadequate during the initial assessment. This calculation, along with the unique requirements of the system, e.g., the light's beam must be spread across the section of the undercarriage in view, informed the redesign. Lastly, the assessment of the control system revealed that the present methods were categorically unfit for real-world inspections. These methods include the nature of the control system and the feedback supplied to the operator. In this case, research was first conducted to inquire how other systems operate in similar conditions, and solutions were

pursued based on market-tested methods. In each case, testing was conducted to validate the areas of redesign, and the process was iterative in most cases.

1.5. Outline

This study will first describe the TCR in detail and assess its existing capabilities regarding the presented operational parameters. This study will then identify key areas requiring redesign and modification. The presented redesign methodologies will be employed to isolate and improve subsystems that do not meet the operational requirements. Testing will then be presented to validate the modifications to the TCR. The results will be presented to prove that the modifications to the TCR have distinctly improved its ability to perform continuous inspections on complete rolling stock undercarriages. The final capabilities of the system and any remaining challenges and design drawbacks will be described and compared to similar systems.

2. Design Details

The TCR is a continuous-track robot. The primary subsystems of the TCR are the frame, drivetrain, control, electrics, lighting, and imaging. Figure 3 shows the major components of these subsystems and their relationships with one another. The frame is constructed of 25.4 mm × 25.4 mm t-slotted aluminum. The frame is 1180 mm long, 375 mm wide, and 250 mm high and, from the side, assumes a trapezoidal shape before modification, as seen in Figure 1. Specific parameters regarding the TCR's drivetrain, electronics, lighting, and imaging systems are summarized in Table 1 and are derived below.

The TCR is driven by two electric skateboard motors (Figure 4a). Each motor's torque is 2.83 Nm, and its maximum continuous current is 80 A. The manufacturer supplied these values [38]. The motors provide power to their respective drive axles at the TCR's left and right upper rear corners through a set of ANSI #25 chains and sprockets. The motor sprocket has 11 teeth and drives a 26-tooth sprocket. An intermediate axle connects this sprocket with a 15-tooth sprocket, which drives a 25-tooth sprocket on the drive axle. Gear ratio is the reduction in rotational speed between the driving and driven sprockets [39]. This ratio is also equivalent to the increase in torque at the driven sprocket. Equation (1) derives the gear ratio.

Table 1. Parameters of the existing Track Crawler Robot design.

Motor torque (each)	2.83 Nm
Max. motor current (each)	80 A
Gear ratio	3.939
Axle material	1566 steel
Axle diameter	15.875 mm
Motor chain size	ANSI #25
Track chain size	ANSI #35
Battery pack	6S2P $LiFePO_4$
Battery nominal voltage	19.2 V
Battery capacity	16 Ah
Battery max. continuous discharge	240 A
Main circuit breaker rating	100 A
Lighting system	4 × light strips: 1800 lumens (lm) total
Lighting power bank	12 V, 6000 mAh lithium
Imaging system	2 × GoPro® Hero8 Black

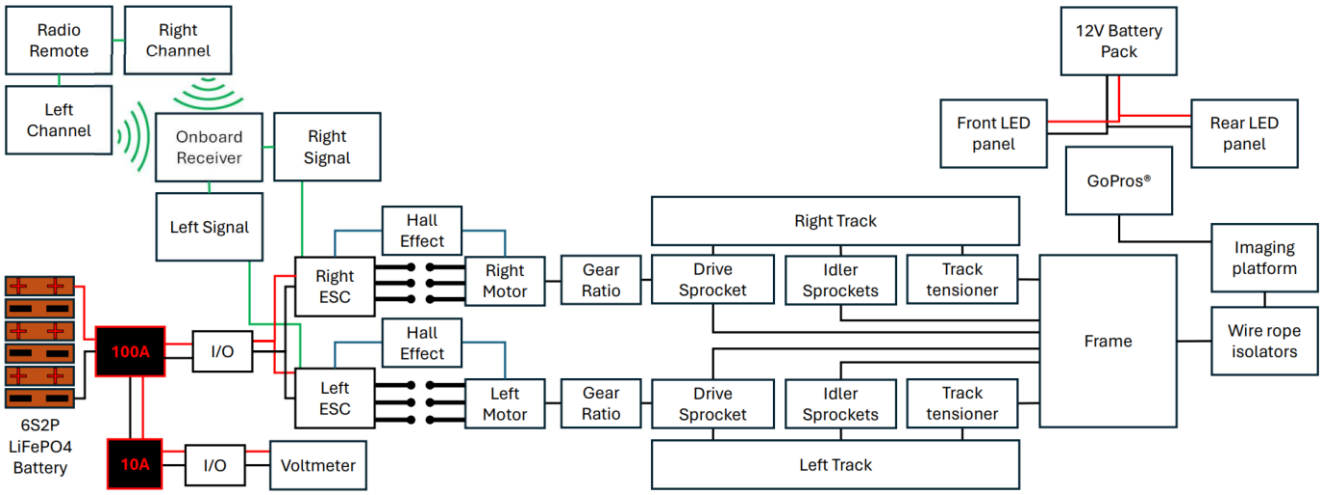

Figure 3. Box diagram showing the major components of the TCR and their relations.

$$Gear\ Ratio = \frac{Driven}{Driving} = \frac{26}{11} \times \frac{25}{15} = 3.939 \tag{1}$$

Using this value, the maximum torque available at the drive axle is defined by Equation (2).

$$T_{driven} = T_{motor} \times Gear\ Ratio = 2.83\ \text{Nm} \times 3.939 = 11.15\ \text{Nm} \tag{2}$$

The maximum working load of the ANSI #25 chain is 620 N [40]. The maximum tensile load within the system can be calculated using the torque at the drive sprocket and the radius at which the force is acting. The pitch diameter is the most effective measurement for this value and is 51 mm for the drive sprocket.

$$F_{max} = \frac{T}{D/2} = \frac{11.15\ \text{Nm}}{(0.055\ \text{m})/2} = 405\ \text{N} \tag{3}$$

Equation (3) shows the maximum force on the ANSI #25 chain to be 405 N, less than the maximum working load. At the output of each drive axle, a pair of 25-tooth ANSI #35 sprockets drive a 76 mm (3 in.) wide modular, chain-driven track with a rubberlike surface molded between two chain links. The sprockets have a pitch diameter of 76 mm. The maximum force within these chains can be found similarly to Equation (3); however, the force value is halved to account for the presence of two sprockets at each axle. Equation (4) shows that the maximum force on each chain of the track will be 147 N, much less than its working load of 2100 N [40].

$$F_{max} = \left(\frac{T}{D/2}\right)/2 = \frac{T}{D} = \frac{11.15\ \text{Nm}}{0.076\ \text{m}} = 147\ \text{N} \tag{4}$$

Therefore, both the ANSI #25 and #35 systems are adequate for the operating conditions of the TCR. Idler sprockets support the track at every alternate corner of the frame. These assemblies consist of two sprockets welded to an axle. The axle is then supported by two ball bearings in a thin-walled steel housing bolted to the frame rails, like the drive axles shown in Figure 4a. An additional idler wheel and tensioner are installed at the top portion of the track to create tension, Figure 1.

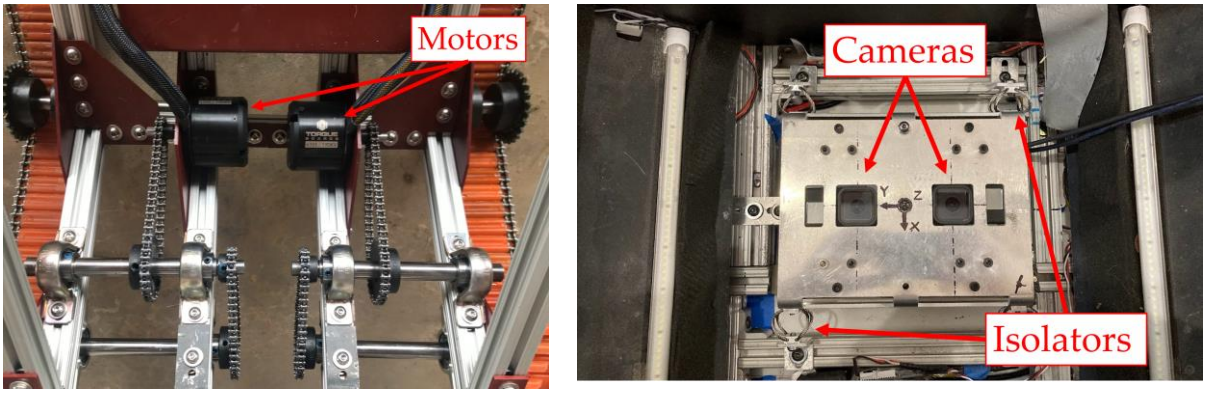

(**a**) (**b**)

Figure 4. (**a**) The drivetrain of the TCR. The respective motors drive independent axles; (**b**) The imaging platform has two vertically mounted cameras supported by wire rope isolators. Two of the four light strips are in view on either side of the platform.

The battery is comprised of $LiFePO_4$ cells in a 6-in-series, 2-in-parallel (6S2P) configuration. Each cell is 3.2 V and has a capacity of 8 Ah. Additionally, each cell is rated for 120 A of continuous discharge. In a battery pack, the total voltage is the voltage of a cell multiplied by the number of cells in series. The capacity and maximum current of the pack are the respective parameters for the cells multiplied by the number of cells in parallel.

$$V_{pack} = V_{cell} \times \#series = 3.2\text{ V} \times 6 = 19.2\text{ V} \tag{5}$$

$$C_{pack} = C_{cell} \times \#parallel = 8\text{ Ah} \times 2 = 16\text{ Ah} \tag{6}$$

$$I_{max,\ pack} = I_{max,\ cell} \times \#parallel = 120\text{ A} \times 2 = 240\text{ A} \tag{7}$$

Equations (5)–(7) show that the system supplies 19.2 V with a capacity of 16 Ah and a maximum continuous current of 240 A. The system is limited by a 100 A circuit breaker.

The motors are controlled using a 6-channel radio remote. Distinct control signals to the two motors are needed for maneuvers such as turning; therefore, the left and right control signals are transmitted independently on two of the channels. The throttle can be controlled manually from −100% to 100% using the vertical position of the remote's joystick. Alternatively, a constant value can be set and applied using a switch on the remote. The throttle signal is duplicated and transmitted on both channels. The steering signal is manually controlled using the side-to-side position of the joystick. The steering signal (positive when to the right) is added to the left control signal and subtracted from the right. This operation then creates a steering signal that remains centered around the desired throttle value. The control signals are received by a compatible receiver onboard the TCR. The receiver contains six three-pin output ports to conduct the signal from each channel. Three-pin connectors are used to transport this signal from the receiver to the three-pin input ports on the respective electronic speed controllers (ESCs). Two ESCs independently control their respective motors, Figure 3. The ESCs receive the control signal and regulate the flow of current to the motors accordingly. The ESCs supply power to the motors through a set of three bullet connectors. Hall Effect sensors feed rotational speed data back from the motors to the ESCs, which can be utilized for PID control. The ESCs run open-source software that allows for customization of control parameters, such as maximum continuous current, control method, and throttle curve shaping. Originally, the ESCs were configured to translate the control signal intensity directly to a motor current; therefore, the operator was responsible for altering the control signal to maintain a constant speed.

The GoPro® cameras, Table 1, are mounted to a platform supported at each corner by a wire rope isolator to dampen vibrations excited within the TCR frame and drivetrain to reduce motion blur caused by vibrations, Figure 4b. As mentioned, a separate power

bank powers a lighting system consisting of four LED light bars. Each LED bar is rated at 450 lumens (lm), leading to a total initial brightness of 1800 lm. Two LEDs are mounted forward of the imaging platform, and two are mounted to the rear, Figure 4b. The power bank operates at 12 V, has a 6000 mAh capacity, and is rated for 3 A. The light bars were tested in a system with a power meter, which found that 25 W were needed to power the system.

$$I = \frac{P}{V} = \frac{25\ W}{12\ V} = 2.08\ \text{A} \tag{8}$$

Equation (8) shows that the lighting system draws around 2 A, which is within the power bank's working range.

Tests are conducted to analyze the existing TCR's capabilities. Imaging tests were performed with the parameters highlighted in Table 2. Two high shutter speeds are used to observe their effect on the image quality while traveling beneath a relatively low imaging target at 10.5 km/h. The linear digital lens was used for this evaluation. The fish-eye lens of the GoPro® naturally introduces a level of image distortion near the edges of the frame, which could decrease the effectiveness of defect detection efforts. The linear lens, however, decreases the FOV to correct for these distortions digitally; for this reason, unless otherwise noted, the linear digital lens was used. The original lighting system was used during the test.

Table 2. Imaging test parameters for the existing TCR.

TCR speed	10.5 km/h
Driving surface	Asphalt
Imaging target	Poster
Imaging target height	0.6 m
Shutter speeds	1/960 s & 1/1920 s
Digital lens	Linear

Figure 5 demonstrates that high shutter speeds effectively reduced and eliminated the motion blur observed in the previous publication and would be necessary for clearly imaging close-up objects while traveling at high speed. The shutter speed used in the previous study was not defined but was clearly set to a lower value. Additionally, the lighting became noticeably dimmer as the shutter speed increased. Videos of the control test using the auto shutter speed, along with the 1/960 and 1/1920 s. tests, are included in the Supplementary Materials.

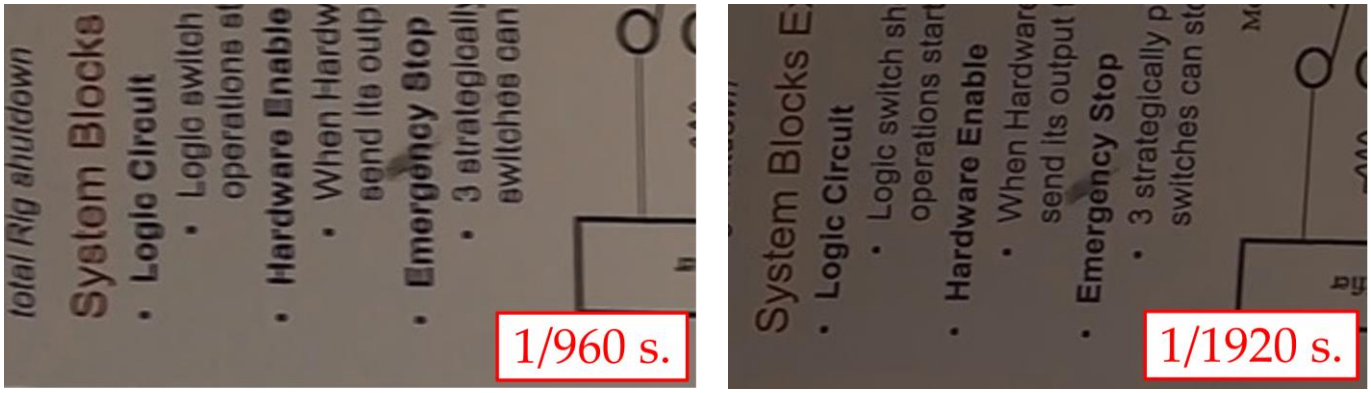

Figure 5. Imaging assessment results at 10.5 km/h with the shutter speeds displayed.

Next, to further evaluate the lighting system's performance in relation to the camera's shutter speed and investigate its ability to adequately illuminate a surface when ambient lighting is dim, a stationary test was performed with the parameters shown in Table 3.

Table 3. Original lighting system test parameters.

Imaging target	Trailer undercarriage
Imaging target height	1.2 m
Shutter speeds	1/120 s–1/1920 s
Ambient lighting	Outdoors, after sunset

This test was conducted on a surface twice as high as the previous imaging test and was conducted after sunset to present challenging but possible lighting conditions during real-world inspections. The images were converted to black and white to accentuate the brightness and contrast of each. Results from this test, Figure 6, showed that decreases in shutter speed did, in fact, increase image brightness, and adequate contrast was not observed until shutter speeds were at or below 1/480 s.

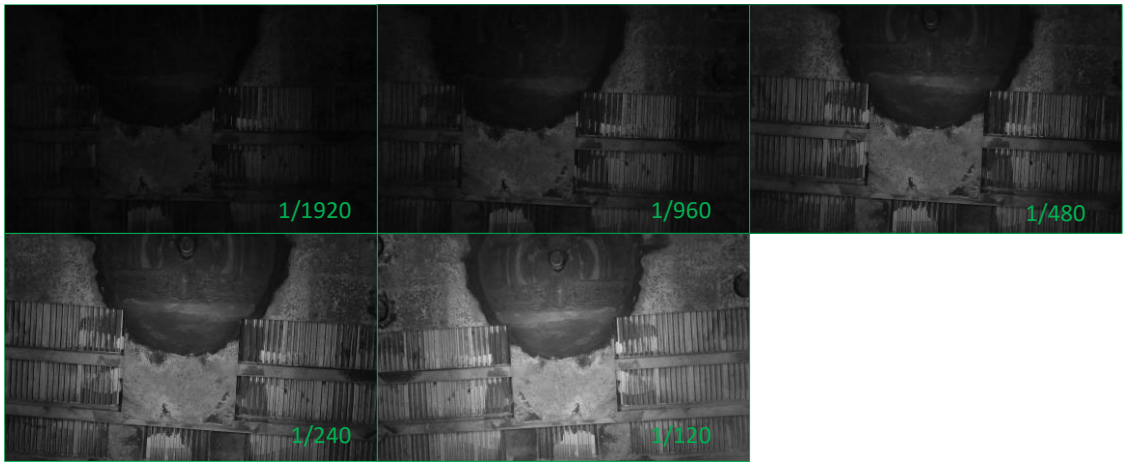

Figure 6. Original lighting system test results. Adequate contrast and brightness are not observed until the shutter speed is at or below 1/480 s.

The existing design's FOV was evaluated by gathering images of a poster with a known-sized grid taken at a height of 380 mm (15 in.), Table 4. The minimum expected component height for hopper railcar gates is about 410 mm; however, the TCR should slightly exceed this threshold to image any unforeseen low-lying components and retain a full FOV when not fully centered within the rails. The dimensions of the resulting image were then measured and used to quantify the extent of the current FOV.

Table 4. Original FOV evaluation parameters.

Imaging target	Grid poster
Grid size	25.4 mm (1 in.)
Imaging target height	380 mm

Figure 7 demonstrates that a maximum of 17 grids (430 mm) could be imaged at this height, representing only 30% of the required 1435 mm width to image the full undercarriage.

Figure 7. Existing field of view (FOV) evaluation image demonstrating an ability to image only 17 grids (430 mm) at the minimum height.

It was then desired that the existing TCR's performance be evaluated while operating in field conditions. To replicate the field environment, a "Test Bed", as seen in Figure 8, was constructed using wooden planks to simulate the ties and gravel to simulate the ballast. Plywood ramps were constructed at each end of the Test Bed, and a sheet of composite board was fastened at the leading edge of each ramp to provide a smooth transition from the ground.

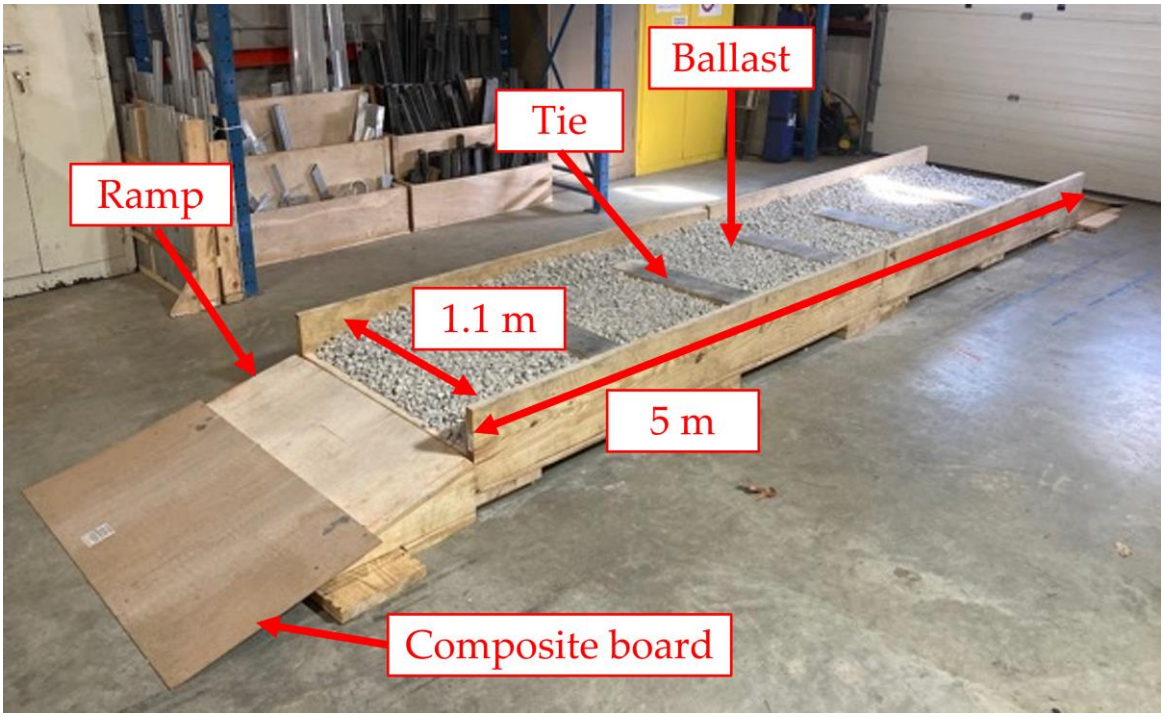

Figure 8. Finalized Test Bed with Dimensions and Components Labeled.

The TCR was driven across the Test Bed at different speeds. Its performance was evaluated using video footage. At speeds below 4.8 km/h, the TCR was observed colliding with the edges of the ties, but the collisions did not appear significant, with a few causing the front end of the TCR to become slightly airborne. However, at 6.8 km/h, the TCR was violently jolted by collisions with ties, and the front end became significantly airborne. A frame from the video is shown in Figure 9a. The difficulty of controlling the TCR through feedforward methods was also revealed during the testing, as the varied terrain made maintaining the speed very difficult. Lastly, video from a camera placed at the end of the Test Bed showed that the undercarriage bearing housings were exposed to impacts from the ballast, Figure 9b. Inspection revealed that these components all had signs of being

impacted, and a few of the bearing housings had become deformed and no longer fixed the bearings and axles in place.

(**a**) (**b**)

Figure 9. Test Bed evaluation results: (**a**) Sharp collision during the 6.8 km/h test, causing the front end of the TCR to become airborne; (**b**) Impact between the ballast and bearing housing.

Conclusions from the Assessment of the Existing Design

As a result of the imaging assessment in Figure 5, it was apparent that a higher shutter speed was key for eliminating motion blur at high speeds. Setting the shutter speed to the maximum value of 1/1920 s effectively eliminated motion blur while traveling up to 10.5 km/h on asphalt—clearer imaging at speeds four times greater than the previous parameters. From the Test Bed evaluations, it was determined that 4.8 km/h was the current maximum speed for reliable and controllable track bed operations, much slower than the operating speed during the shutter speed evaluation on asphalt; however, the track bed could introduce motion blur at lower speeds due to the increased vibration. Therefore, it was determined that 1/1920 s would be the operating shutter speed of the TCR. Additionally, from the FOV evaluation in Figure 7, it was evident that the imaging system could not image a 1435 mm width at a height of 380 mm and was only capable of capturing 30% of the required width. Modeling the current FOV in comparison with the required, as shown in Figure 10, revealed that imaging the entire undercarriage with a single camera as configured would be impossible; additionally, components of the frame and track assemblies were located between the imaging platform and portions of the undercarriage. Therefore, modifications to the frame, track, and camera configurations were necessary to provide the TCR with the capability to image a railcar's undercarriage fully.

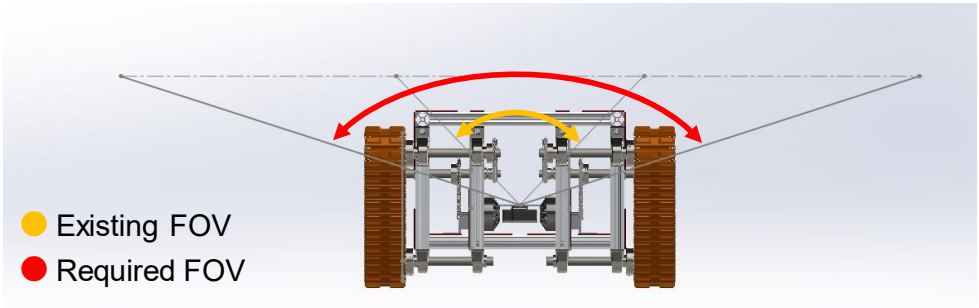

Figure 10. Existing FOV compared to the required FOV.

From the lighting evaluation in Figure 6, it was observed that the brightness in the image increased as the shutter speed decreased. This was because, as the shutter speed decreased, the time of exposure increased, allowing more light to reach the sensor during each frame and brightening the image. Adequate brightness and contrast were absent until

the shutter speed reached values at or below 1/480 s, four times less than the required 1/1920 s.

Therefore, it was determined that an increase in lighting of at least four times would be required to image at 1/1920 s. Additionally, it was determined that more brightness beyond that threshold would be required to adequately illuminate the far lateral regions of the FOV, as the original lighting focuses most of its light on the overhead area.

Evaluations of the TCR's mechanical design revealed that the idler sprocket assemblies were inadequate for continuous operation in the track bed. To improve the TCR's reliability, these assemblies should be redesigned and modified.

Lastly, the Test Bed evaluations revealed the difficulty of feedforward control in the track bed environment. Operators would have to constantly vary the throttle of the TCR to maintain a constant testing speed; therefore, it was determined that feedback control should be implemented in place of the existing feedforward control. Lastly, it was determined that a method for providing the TCR operator with a real-time video feed from the TCR was necessary for controllability during real-world inspections as the TCR passes out of view periodically.

3. Design Improvements

3.1. Field of View Redesign

Portions of the frame needed to be relocated to remove their obstruction from the required FOV while maintaining strength and functionality. A 3D model of the imaging platform was created with an array of potential camera mounting angles to quantify the area needing to be cleared. The FOV of each camera was physically modeled using the "SuperView" digital lens, which maximizes the FOV of the camera but introduces image distortion around the edges. Using the digital lens with the maximum FOV in the model ensured that, if needed, the SuperView lens could be used without picking up portions of the frame in the image. The model was then used to verify that the proposed camera mounting locations spanned the required FOV, Figure 11a, and when extrapolated out to the width of the frame, it highlighted where intersections occurred, Figure 11b.

Based on these findings, two concepts were drafted, which relocated frame members outside the required area, Figure 12. The first one, "Concept A", shown in Figure 12b, consists of angled frame members bracketing the newly cleared area with a horizontal frame member between the two. Concept B, shown in Figure 12c, consists of frame members stretching vertically downward at the edge of the cleared area, with a similar frame member stretching across the resulting gap.

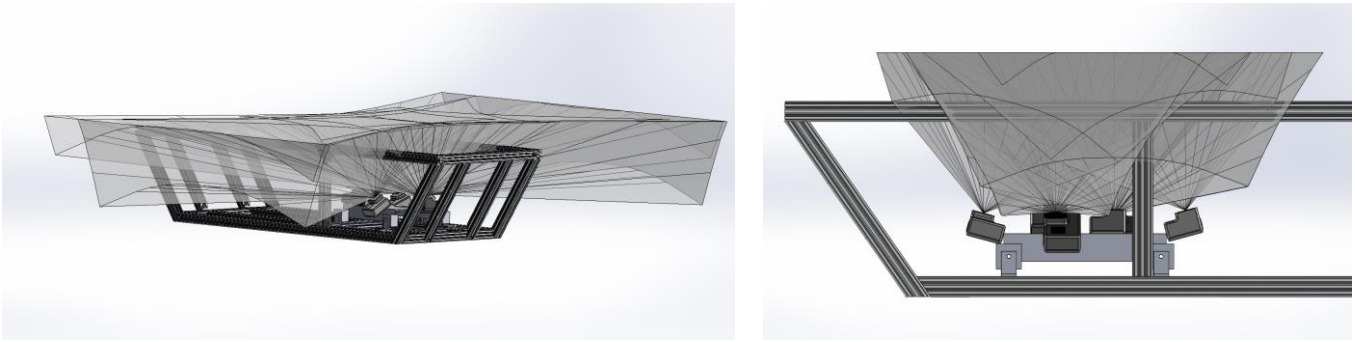

(**a**) (**b**)

Figure 11. Original TCR frame modeled with sample camera setup: (**a**) Camera FOVs extrapolated out to a 1435 mm width and 380 mm height, illustrating the ability to span the required FOV; (**b**) Camera FOVs cut to the width of the TCR to highlight the areas of intersection.

(**a**) (**b**) (**c**)

Figure 12. Side view of the TCR frame: (**a**) Original design; (**b**) Concept A, angled frame member redesign; (**c**) Concept B, vertical frame member redesign.

A relative FEA analysis was conducted in SolidWorks Simulation between the concepts and the original design to aid in choosing between the two. The xz-plane cross-section of each was subjected to a load meant to simulate an impact with a tie. The load was 600 N applied at 60° from the ground plane. The load was transmitted through the bottom surface of the leading, angled frame member to approximate the load traveling into the frame from the leading sprocket assembly colliding with a tie. The lower horizontal frame member was constrained by fixing the cross-section of each end in space but allowing for rotation to allow flexure under loading. Roller/bearing constraints supported the lateral faces of the top horizontal beams. These fixtures were chosen to constrain the frame within the xz-plane. The study sought to quantify each concept's relative strength in this plane since it includes most of the loads applied to the frame and other components. The frame was modeled as 6061 aluminum. In reality, the framing is 6105 aluminum; however, the two alloys are very similar and share similar yielding and tensile strengths [41]. The performance of the parts was quantified using the factor of safety (FOS). The FOS defines the ratio from the simulated condition within a part to its hypothesized failure criterion, i.e., when the FOS is 2, the condition within the part used to predict failure is at half the intensity of where failure can be expected. In this case, the Von Mises Failure Criterion was used. Von Mises predicts failure when distortion energy per unit volume within the part exceeds a certain threshold. Equation (9) defines this criterion in terms of the principal stresses within the part and the tensile yield stress of the material [42].

$$\left(\sigma_1^2 + \sigma_2^2 + \sigma_3^2\right) - \sigma_1\sigma_2 - \sigma_2\sigma_3 - \sigma_1\sigma_3 = \sigma_y^2 \tag{9}$$

Figure 13 shows the FOS results for the original frame design. The pink line shows the beam fixed in place but allowed to flex. The pink arrows in the left corner represent the application of the forces, and the green arrows show the location of the roller/bearing fixtures on the top beam. Blue is used to represent any area with a FOS above 5. Red is used to represent a FOS at or below 1, and a gradient is used for the values in between. Three comparable locations of each concept dropped below a FOS of 5: inside the leading corner (Location 1), within the bottommost beam (Location 2), and at the corner of the leading vertical support (Location 3). The lowest FOSs for each location have been tabulated in Table 5.

Table 5. Factor of safety comparison between each frame concept.

	Location 1	**Location 2**	**Location 3**
Original	1.11	3.28	2.60
Concept A	1.16	3.47	2.03
Concept B	1.21	3.37	1.71

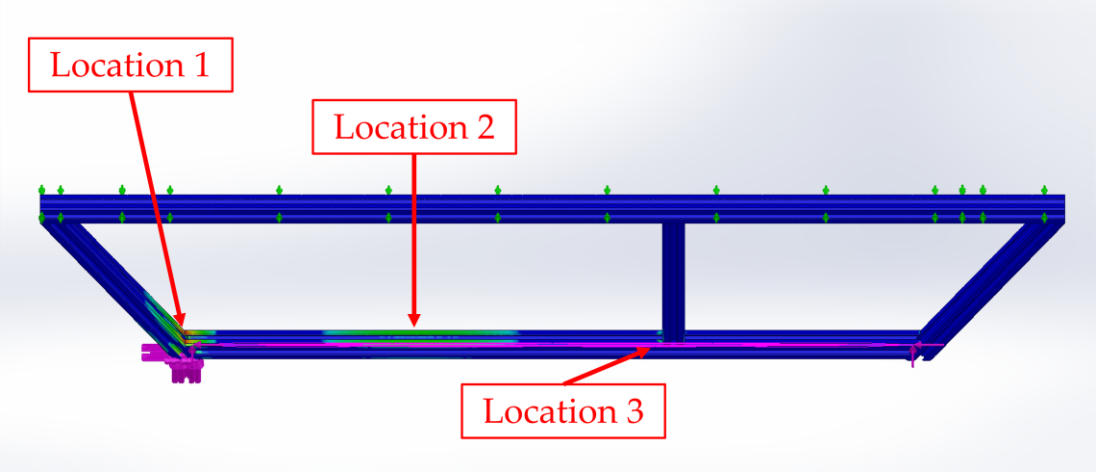

Figure 13. The factor of safety results for the original frame design with the stress concentration locations labeled.

Concepts A and B outperform the original frame's minimum FOS of 1.11, with Concept B marginally outperforming Concept A. However, at the two other locations, Concept A outperforms Concept B. This fact, combined with slight weight savings from Concept A and engineering judgment, led to the conclusion that Concept A should be chosen.

A modal analysis was then conducted using ANSYS to evaluate how the inclusion of Concept A affected the modal response of the frame as a whole, Figure 14. The lowest meaningful mode for the original and redesigned frame was torsion about the *x*-axis. The original frame was excited into this mode at 74 Hz, while the redesign had a decreased mode frequency of 67 Hz, indicating a decreased stiffness. This was expected due to the lack of a continuous top frame member. It was desired to increase the natural frequency of the modes to demonstrate an increase in the overall stiffness of the frame. Therefore, a set of transverse frame members was included in the model, spanning the width of the frame between both angled frame members, bracketing the FOV window, Figure 14c, and the modal analysis was conducted again. After this inclusion, the lowest mode frequency was raised to 80 Hz. The mode shape appears to be similar to the original torsional mode but is slightly altered. The redesigned frame had now been shown to be as strong and stiff as the original design and was finalized.

To route the track below the window created by the redesigned frame, the tensioner and idler wheel assemblies were relocated, Figure 15. The tensioner was mounted to the front angled frame member with its spring fixed to the bottom of the frame, and the idler wheel was mounted to the rear angled frame member at a level, ensuring that the track remained out of the FOV across the entire width of the window while retaining the functionality of both assemblies to maintain tension on the tracks.

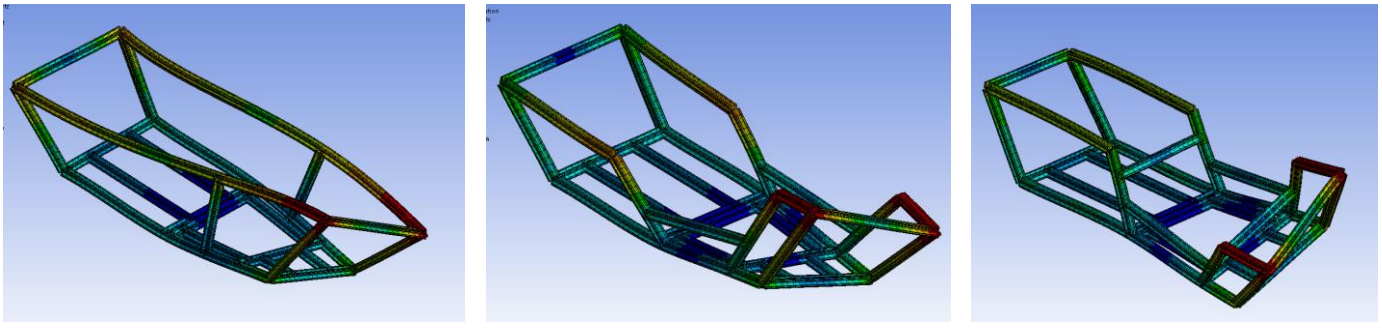

(**a**) (**b**) (**c**)

Figure 14. Lowest frequency mode shape for each frame iteration: (**a**) Original frame, 74 Hz; (**b**) Redesigned frame, 67 Hz; (**c**) Redesigned frame with transverse frame members added, 80 Hz.

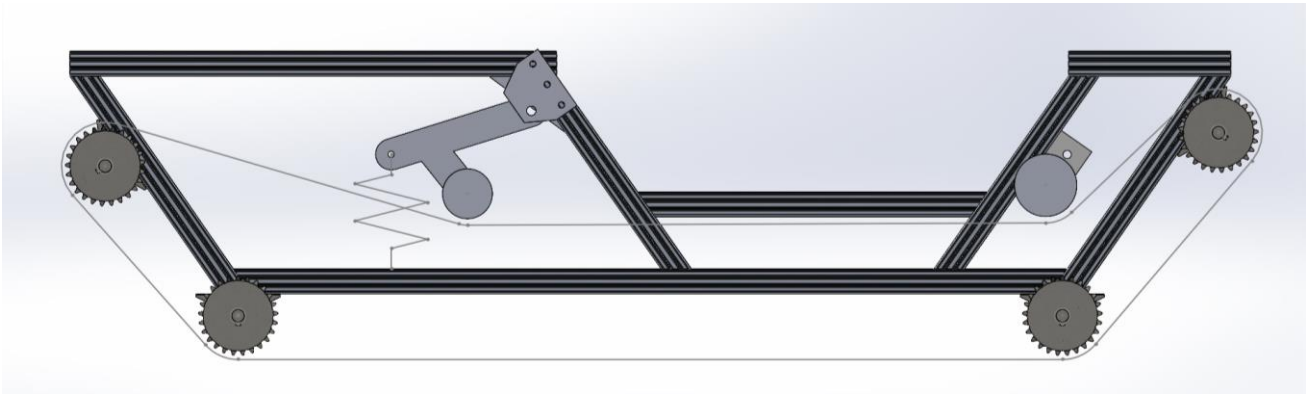

Figure 15. Relocated positions of the tensioner and idler wheel assemblies to route the track around the frame window.

To modify the frame according to this redesign, the topmost frame members were cut into two pieces, and the new frame members were installed using custom-cut aluminum brackets, Figure 16a. The light strip panels were installed onto the surface of the transverse frame members to locate them in a similar position. Lastly, one of the vertically oriented cameras was removed and replaced by two additional cameras, angled toward the left and right sides, Figure 16b.

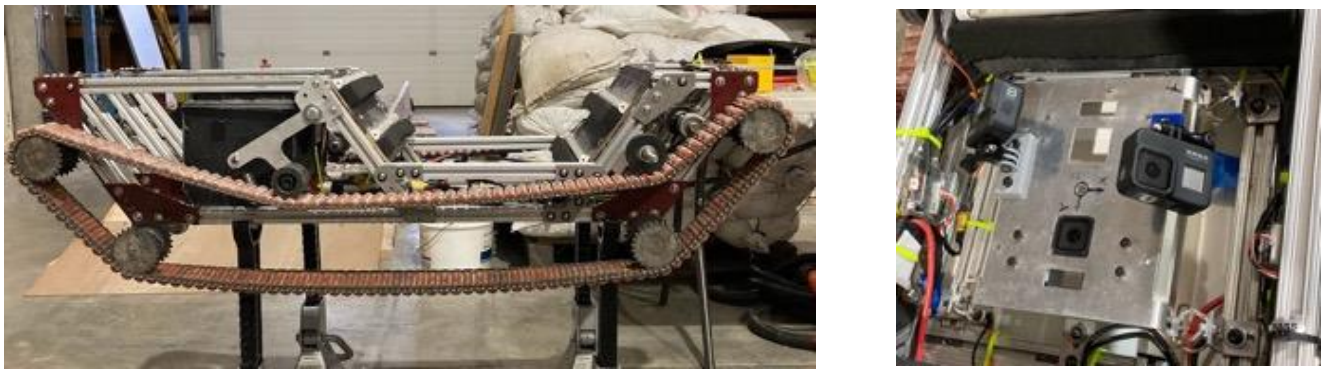

(**a**) (**b**)

Figure 16. Completed FOV modifications: (**a**) Redesigned frame and track configurations; (**b**) Redesigned camera configuration, taking advantage of the newly available FOV.

3.2. Lighting System Redesign

As noted, adequate contrast and brightness were not observed in the imaging test until the shutter speed had been decreased by a factor of four from the target value. The original four LED light strips output a total of 1800 lm; therefore, the overhead lighting should be capable of at least 7200 lm and likely more, as this level of light is required across the entire FOV, where the original lighting focuses most of its light on the overhead area.

To meet this requirement, a set of two LED light bars, Table 6, was chosen due to their high output, floodlight lens to spread the beam across a wide area, and low-profile design. Together with the original system, these light bars brought the total intensity of the system to 12,200 lm, nearly seven times the original intensity. They were wired into the main circuit of the TCR using a voltage converter, as the power was too great for the power bank used by the original lighting system. The light bars were initially mounted on the outside of the frame, just below the window, to provide lighting to the overhead and lateral regions of the FOV, Figure 17.

Table 6. Improved lighting system parameters.

Intensity (per bar)	5200 lm
Power (total)	120 W
Light bar voltage	12 V
Voltage converter efficiency	<90%
Estimated current draw	6.9 A

Figure 17. Initial configuration of the additional light bars.

3.3. Idler Sprocket Assembly Redesign

To relocate vulnerable components from the TCR's undercarriage, idler sprockets with integrated bearings were deemed a potential option since housing them within the sprockets would effectively shield them. A concept was created utilizing the same 15.875 mm diameter shafts, Table 1, with compatible cast iron shaft mounts that clamp onto the shafts, preventing sliding and rotation. Twenty-tooth ANSI #35 ball-bearing idler sprockets could be placed onto the shaft and located using retaining rings, Figure 18. The only components exposed to direct impact in this design are the cast iron shaft mounts and a small portion of the fixed axle. These are solid metal components, much more durable than the exposed bearings and housings in the previous configuration.

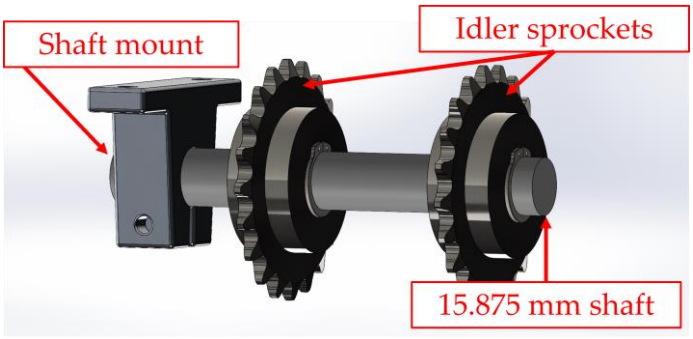

Figure 18. Model of the proposed idler sprocket assembly.

To investigate the validity of this design, an FEA study was conducted on the shaft and mount to simulate their response to a significant collision with a tie. The shaft was fixed spatially and rotationally to simulate its condition within the mount. The mount was constrained with two fixed fixtures applied to the inside of the bolt holes. Roller/bearing fixtures were applied to the surfaces above and below the bolt holes to simulate the clamping supplied by the bolt. Lastly, a bearing fixture was placed on the face of the mount opposite the sprockets to approximate the effect of a plate welded to the back of the mount and bolted to the frame to aid in moment transfer. This plate was later removed from the concept, but its inclusion in this study was deemed insignificant as the main investigation points were the shaft and the mount.

The forces were derived from video and chassis-mounted accelerometer data recorded during a large collision with a tie at approximately 8 km/h on the Test Bed. The absolute maximum x-direction deceleration during the collision was found to be 2.8 G.

$$F = ma \tag{10}$$

Using Newton's second law of motion, Equation (10), the force in the x-direction was found to be 1290 N, given the TCR's weight of 47 kg. Next, the z-directional force was found by equating force to the energy imparted into the system over some distance, Equation (11), with the distance approximated by the impact time and the nominal velocity.

$$F = \frac{\Delta E}{\Delta d} \approx \frac{mg\Delta y}{V\Delta t} \tag{11}$$

From the accelerometer data, the collision length was found to be 0.017 s, and the center of gravity was raised approximately 50.8 mm (2 in.) due to the collision. This calculation led to a z-directional force of 611.3 N, which tripled to 1834.9 N to approximate the maximal impact force. These resulting forces were then halved to share the collision forces across both axles, leading to −645 N applied in the x-direction and 917.45 N applied in the z-direction.

The FEA results, shown in Figure 19, show that the shaft has a minimum FOS of 4.5, indicating a strong ability to endure this load case. The mount, however, has a minimum FOS of 0.74, with a ring of low FOS locations lying at the edge of the interface between the shaft and the mount. Yielding at this location will only increase the bearing surface area and should, therefore, remain local, not posing a risk of buckling or heavily deforming the part; hence, the assembly was deemed adequate and was finalized.

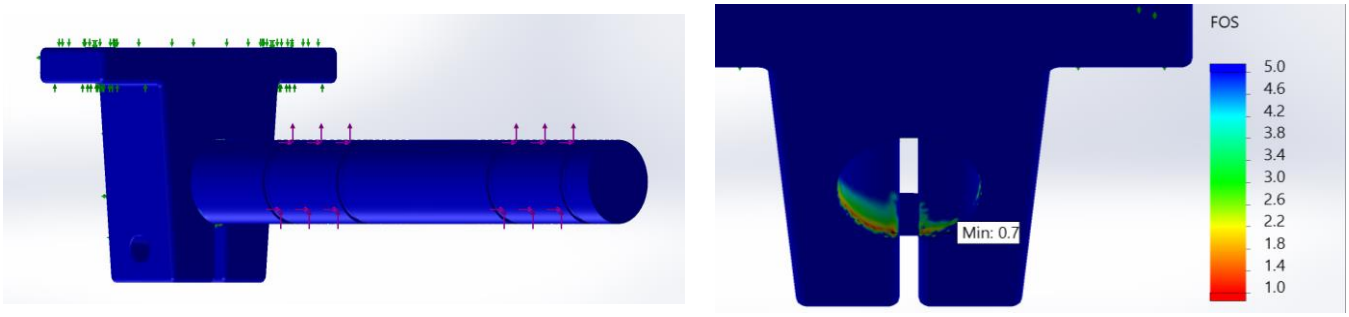

(**a**) (**b**)

Figure 19. Idler mounting assembly FOS plot: (**a**) Assembly of mount and shaft showing the forces (pink arrows) applied at the idler sprocket locations and the fixtures (green arrows) applied at the top and bottom bearing surfaces and the back face of the mount; (**b**) A stress concentration is shown on the inside face of the shaft mount.

In hindsight, the configuration of fixtures in this study hid stress concentrations due to moments about the bolted joints, a weakness that would be revealed; however, this study was initially used to validate the design.

The shafts were cut to length and turned on a lathe to create the retaining ring grooves. The sprockets were then installed on the shafts bracketed by retaining rings, and the shafts were fixed in the mounts such that the installed sprockets lined up laterally with the drive sprockets. The assemblies were then fastened to the frame rails using #10−32 bolts and specialty nuts designed to clamp onto the t-slots, Figure 20. The resulting assembly decreased the total weight of the TCR by over 4.5 kg.

Initial testing on the track bed revealed that the #10−32 nuts used to secure the assemblies to the frame rails were insufficient. A set of nuts split in two, Figure 21a, and most others were deformed. This failure was most likely due to the large stresses from moments and this weakness being suppressed by the fixtures in the FEA study. The

assembly hardware was, therefore, upgraded to Grade 8, 1/4-in.−20 bolts, Figure 21b, which increased the tensile area by over 80% [43]. Additionally, rather than clamping onto the t-slots of the frame, through-holes were drilled to clamp across the entire beam, allowing for more effective moment transfer. Additionally, standard hex nuts could be used in this configuration, eliminating the thin-wall failure mode of the first design.

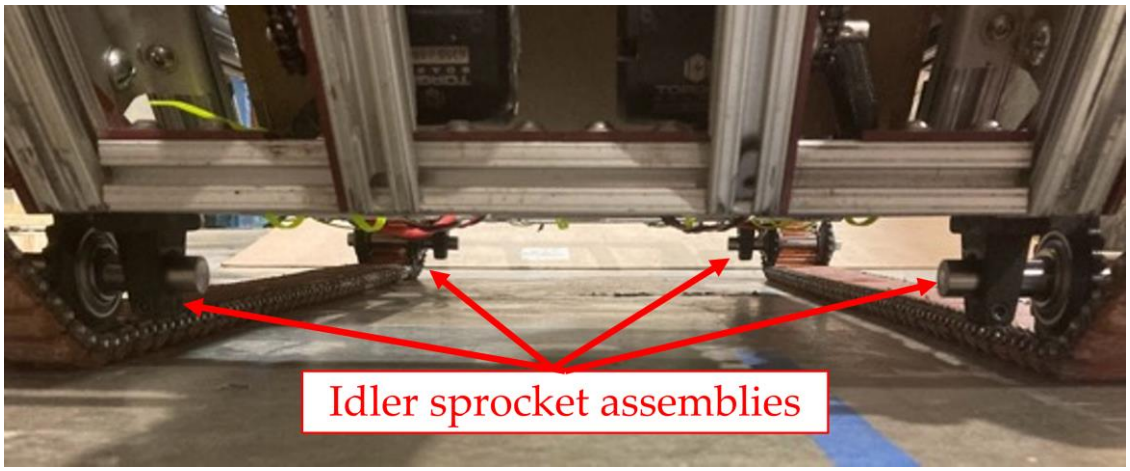

Figure 20. Finished installation of redesigned idler sprocket assemblies.

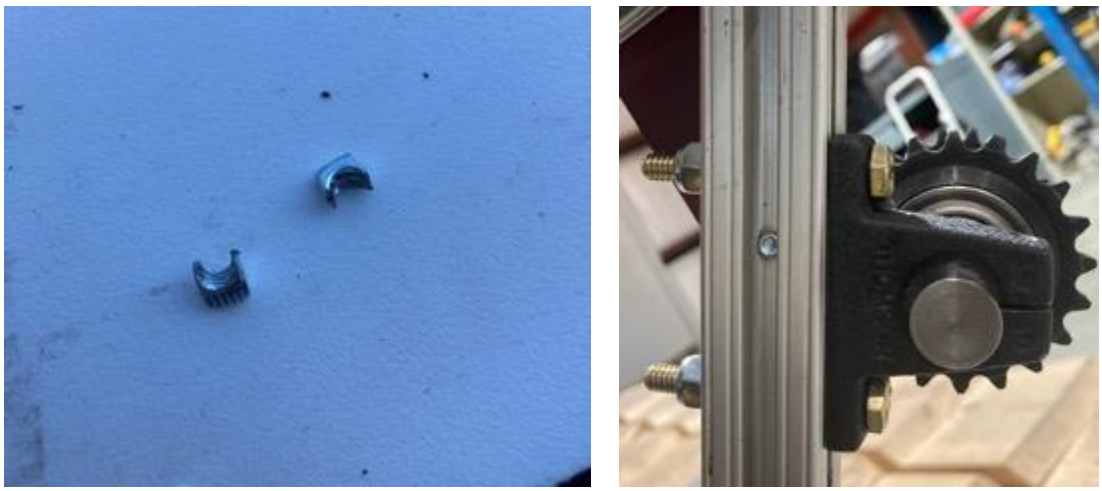

(**a**) (**b**)

Figure 21. (**a**) Split #10-32 mounting nuts from the validation test; (**b**) Improved mounting configuration using 1/4-in.−20 hardware.

3.4. Control System Redesign

Under feedforward control, the Test Bed was causing large speed fluctuations and stalls during testing as the resistance to forward motion varied greatly. To maintain a constant speed in these conditions, feedback control was necessary. The Hall effect sensors in the motor were connected to the ESCs, which include support for PID control. With the sensors connected, the ESCs could read the motor's speed, and PID control was configured. PID control operates by using three tunable parameters to guide the system's response to errors between the system's response and the commanded signal. Equation (12) shows the standard form for a PID controller.

$$C(s) = K_p + \frac{K_i}{s} + K_d s \tag{12}$$

The proportional term, K_p, increases the control response as the instantaneous error grows. The integral term, K_i, tracks the error over time and alters the control signal to drive it to zero. The inclusion of this term drives the steady-state error to zero for step inputs. Lastly, the derivative term, K_d, responds to the rate of change of the error. This term helps to decrease large overshoots above the desired value. Table 7 shows the parameters utilized in this system.

Table 7. PID controller parameters.

K_p	K_i	K_d
0.005	0.003	0.00005

The control signals from the radio remote were now mapped to speeds. The ESCs regulate motor effort to maintain the commanded speeds. This control method increases the repeatability of testing and simplifies operation, allowing the operator to focus on other tasks.

It was also determined that a method for providing the operator with real-time video footage from the TCR to serve as control feedback should be included in the design. First-person view (FPV) camera systems are extensively used in the drone market to stream real-time footage from an onboard camera to a monitor at a very low latency (<50 ms) [44]. Adding such a system to the TCR would allow the operator to always view the TCR's heading and position, providing the necessary information for timely and precise steering inputs.

To add the FPV system to the TCR, a small FPV camera and transmitter combination were purchased, along with a small monitor compatible with the camera's transmission frequency of 5.8 GHz. Lastly, rechargeable 3.7 V lithium batteries were purchased to power the camera and transmitter. With 2000 mAh of capacity, one battery could power the 500 mA camera for approximately 4 h, much longer than a standard inspection.

The FPV camera was mounted at the front of the TCR between two frame members, Figure 22, to capture a useful camera angle while remaining protected by the frame. A mount was 3D printed to locate the camera and battery in place, with a dome added to protect the camera's antenna. Initial operations revealed that the camera built up heat rapidly during operation. This may be suitable for use on drones, as rapid ambient air passing the camera will effectively cool the device, but the speeds of the TCR are too low for this to be the case. Therefore, a 12 V fan with an 11.1 V LiPo battery was included on the mount next to the camera to provide active cooling during operation. The monitor was mounted onto the radio remote for convenient viewing while operating the TCR.

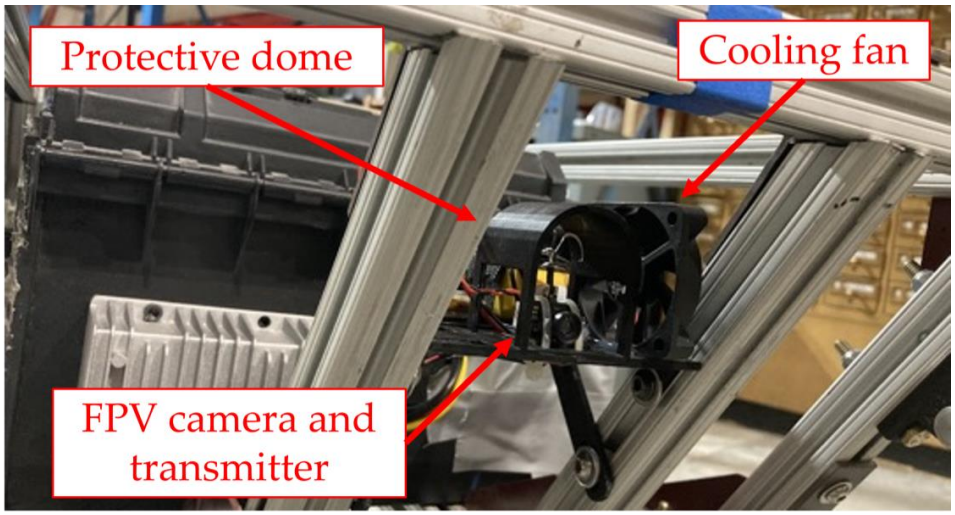

Figure 22. FPV camera mounting location at the front of the TCR.

4. Test Setup

4.1. Field-of-View Test Setup

To evaluate the ability of the TCR to image the full FOV, a similar test to the initial assessment was conducted, Table 4, imaging the grid poster. Of note, the width of this poster is 1520 mm, exceeding the overall width required for full FOV imaging. Therefore, if the side-view camera angles could image the edges of the poster while also overlapping with the FOV of the vertical camera, it would validate that the modified system was capable of imaging an entire railcar undercarriage. The TCR was centered beneath the poster, and videos were recorded from all three cameras in identical arrangements as would be seen during inspections. The FOVs of the resulting videos were then analyzed.

4.2. Image Quality Evaluation Test Setup

A preliminary image taken with the improved lighting system suggested that, although floodlights, the light bars may be behaving as spotlights due to the extremely short distance from the light bar to the level of low-lying components. Therefore, a series of tests were conducted to evaluate the overall performance of the lighting system and experiment with the effects of various diffusive coverings, Table 8. It was desired to determine which method best illuminated the full FOV while maintaining an acceptable level of intensity.

Table 8. Tested diffusive coverings.

Control	N/A
Covering 1	2 layers of wax paper
Covering 2	Frosted plexiglass
Covering 3	Combination of wax paper and plexiglass

To complete this test, a pickup truck undercarriage was used to approximate the railcar undercarriage. The pickup truck was driven onto 30.5 cm (1 ft.) blocks over an indoor concrete floor to simulate the approximate height and width of typical rolling stock undercarriage components, Figure 23a. Imaging data was taken from all three cameras while the TCR traveled at 4 km/h, and the diffusive coverings were placed over the light bars as shown in Figure 23b. The resulting images were analyzed for adverse lighting effects such as dim areas and glare to draw conclusions about the effectiveness of each diffusive covering.

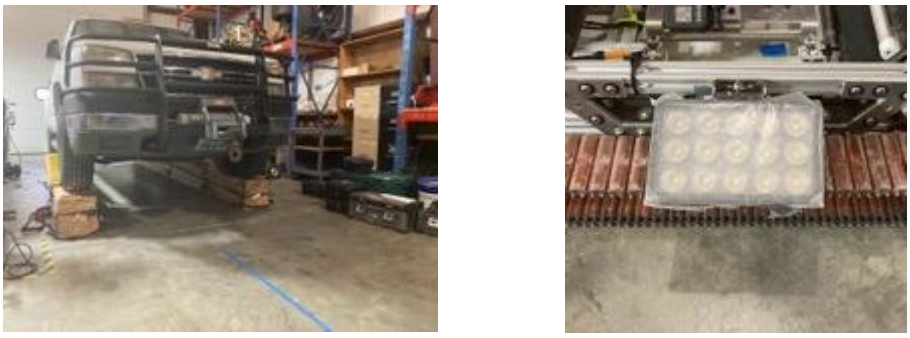

(**a**) (**b**)

Figure 23. Under-truck testing setup: (**a**) Pickup truck placed on 30.5 cm high blocks; (**b**) A sample diffusive covering, two layers of wax paper.

Next, the TCR was tested beneath an outdoor tractor-trailer. This test evaluated the lighting and imaging system's robustness to similar FOV and lighting conditions that will be seen during real-world inspections. The tests were performed at 9.6 km/h, which also tested the ability of the system to reject motion blur at speeds twice the attainable track bed

speed. The combination of wax paper and plexiglass was used for diffusion. Additionally, before this testing, the light bars were relocated to be mounted to the frame's interior just forward of the imaging platform. This was performed to mount the light bars in a location where they were shielded by the frame of the TCR rather than exposed on the sides. For these tests, they were oriented vertically, Figure 24. The TCR was placed a short distance behind the trailer. This allowed the TCR to reach testing speed before traversing beneath the trailer. A step input was applied to command the testing speed, and manual steering inputs were applied by the operator to account for any deviations from the desired course. Videos were recorded from all three onboard cameras.

Figure 24. The setup for under-trailer testing. The light bars were relocated to the front transverse frame member and oriented vertically.

4.3. Mobility and Reliability Test Setup

A series of tests were conducted at a local set of tracks to evaluate the mobility and reliability of the TCR. These included a general mobility test, which evaluated the TCR's ability to climb over the rail into the track bed, perform a 180° differential steering turn, and climb out of the track bed again. A series of constant speed tests were also conducted, described in Table 9, designed to evaluate the TCR's performance at speeds within the operating limit of 4.8 km/h determined during the initial evaluations on the Test Bed.

Table 9. Constant speed test parameters.

Speeds tested	1.6, 3.2, and 4.8 km/h
Test length	25 m
Tests per speed	2
Surface	Track bed

Video footage was taken from the trackside to visually monitor the TCR's performance, and real-time battery current, motor current, and speed data were gathered from both ESCs during each test.

4.4. PID Control System Evaluation

During the mobility and reliability testing at the local tracks, the PID control system was evaluated. Each constant speed test was conducted by applying a step input of the desired testing speed. The system's response during the transient portion of these tests was analyzed to evaluate its step response. The system's ability to maintain testing speed in the

high-disturbance track bed environment was evaluated, and key metrics, such as the rise time, were calculated. Motor speed data was gathered from the ESCs via Bluetooth.

4.5. First-Person View System Evaluation

Tests were conducted to evaluate the viability of the installed FPV system. First, to test the ability of the system to provide adequate feedback at a low enough latency, the TCR was driven across the length of the Test Bed at 4.8 km/h using only the FPV system to provide feedback for manual steering inputs. The test was used to qualitatively evaluate the effect of latency on the ability to control the TCR at the current maximum operating speed in the rough Test Bed terrain. This test also evaluated the system's robustness to vibration and whether it would degrade the image to the point of uncontrollability.

Another set of tests was conducted to evaluate the effectiveness of the FPV system for control during under-trailer testing. These tests evaluated the ability of the FPV system to operate under similar lighting conditions as seen beneath the rolling stock. Tests were operated at speeds up to 9.6 km/h, further evaluating the effects of the system's latency on overall controllability.

5. Results and Discussion

5.1. Field-of-View Validation Results

After the modifications to the frame, track routing, and camera configuration, the tests indicate that the TCR is capable of imaging a full rolling stock undercarriage in a single pass. Figure 25 shows that the left camera angle can image the far edge of the 1520 mm wide poster mounted at 380 mm while also overlapping with the FOV of the vertically oriented camera. This result demonstrates that the FOV now spans the entire 1435 mm width at 380 mm, and the TCR's FOV has been increased from just 30% of the required to 100% while still using the linear digital lens. Therefore, without any image distortion, the TCR will be able to provide an image of the entire railcar undercarriage. This capability is crucial to the development of the TCR, as the risk of not imaging a defect that should be visible from the undercarriage is greatly reduced.

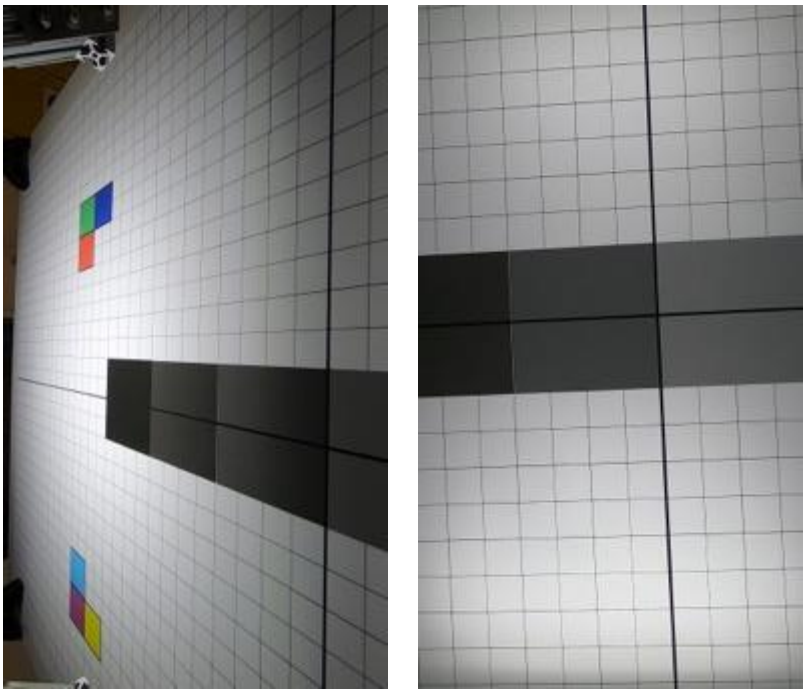

(**a**) (**b**)

Figure 25. FOV validation results show the ability to image from the center to the far edge of the 1520 mm poster: (**a**) Left view; (**b**) Vertical view.

5.2. Image Quality Validation Results

Results from diffusion method testing under the pickup truck show that diffusers aid in reducing the intensity and presence of harsh reflections, Figure 26. The combination of frosted plexiglass with two layers of wax paper does so most effectively and nearly eliminates pixel saturation in the case of the muffler, Figure 26d. The added diffusion provides more light to the outer reaches of the FOV and helps to prevent the camera from reducing its sensitivity in response to bright reflections, causing a two-fold increase in image quality. Additionally, the overall intensity of the light is not significantly reduced by the diffusive coverings, Figure 27. Therefore, diffusers were included in the TCR design, and for the remainder of the imaging tests, a combination of frosted plexiglass and two layers of wax paper was installed. Areas of glare are still possible in this configuration; however, the effect is mostly limited to close-up, reflective objects, such as the axle in Figure 28a.

(**a**) (**b**) (**c**) (**d**)

Figure 26. Comparison of diffusion methods on glare reduction from mufflers: (**a**) No diffusers; (**b**) Wax paper; (**c**) Plexiglass only *; (**d**) Plexiglass and wax paper. * Different color settings were used in other tests.

(**a**) (**b**) (**c**)

Figure 27. Under-truck images highlighting the image quality and absence of harsh reflections from metallic surfaces: (**a**) Side view showing metal pipe without major reflections; (**b**) Vertical view of a low-lying beam with well-lit components above it; (**c**) Side view showing adequate lighting out to the width of the wheels at the height.

Images taken of the undercarriage of the pickup truck using the chosen set of diffusive coverings indicate an excellent ability to light and image a wide FOV at close range. The images were well-lit and clear across the entire undercarriage of the truck out to the width of the truck's wheels, Figure 27c. The width between the wheels is similar to the rail gauge, and the wheels are mounted at a height of 305 mm. Therefore, these results also show the ability to image with a greater FOV than required with adequate lighting. Adverse lighting conditions may still occur in the case of occluded areas where shadows may result, Figure 27a. This effect is due to the fact that the light source and camera lens are not in the same location; therefore, the camera is able to image areas that are occluded by the light source, resulting in shadows. Videos have been included in the Supplementary Materials, showing the results of the final lighting configuration compared to the original.

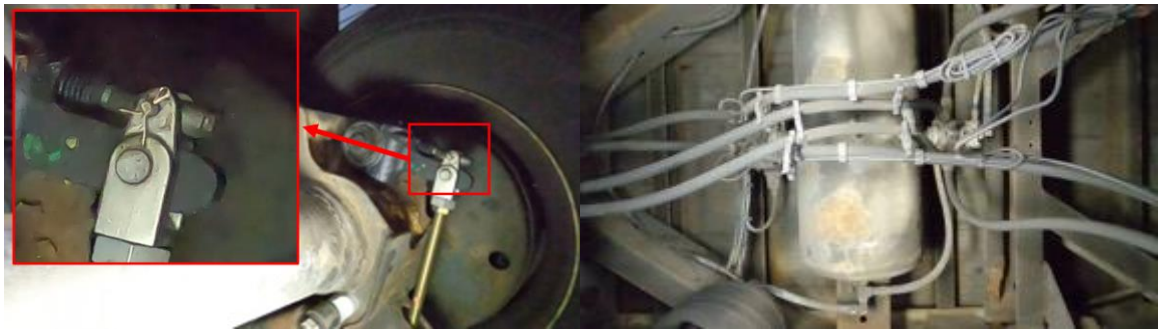

(**a**) (**b**)

Figure 28. Under-trailer testing results: (**a**) Image showing the ability to resolve objects as small as retaining pins while traveling at 9.6 km/h; (**b**) Overhead image showing adequate light quality and image clarity.

From the images gathered beneath the trailer at speeds of 9.6 km/h, it can be observed that the TCR is able to effectively image objects as small as a retaining clip in the brake assembly without any noticeable motion blur, Figure 28a, representing an ability to capture excellent detail while traveling at high speeds and experiencing vibrations. Similar pins are present on rolling stock, and the ability to detect the presence or absence of them while traversing continuously would be very beneficial to the railroads. The images show the ability of the lighting system to adequately light overhead objects (Figure 28b) and objects located laterally (Figure 28a). The results from this test and the previous ones prove the capability to image an entire railcar in a single pass with adequate clarity and lighting. The undercarriage robot developed by Chiaradia et al. [34] can image components from multiple angles using its articulated arm, whereas the TCR can only gather a single angle, creating the possibility for blind spots. However, this robot cannot match the single-pass efficiency of the TCR. Inspectors will not have the time to manually traverse each component of interest and control an articulated arm to gather multiple views. In pre-departure inspections, inspectors need an efficient, reliable method for gaining a clear point of view of the entire undercarriage. The TCR could help identify many more undercarriage defects than is now possible during pre-departure inspections, and technologies, such as the previously mentioned robot, may be suitable for maintenance-point inspections where efficiency is not as great of a concern. Videos have been included in the Supplementary Materials, showing footage of an under-trailer test from each camera angle.

5.3. Mobility and Reliability Test Results

Attempts to use differential steering to complete a 180° turn within the tracks were successful; however, losses in traction on the ballast and insufficient power at times made this process iterative and time-consuming, taking a total of 30 s. Figure 29 shows the motor current and speed data recorded from the left ESC during the full length of the turn.

The turn was performed counterclockwise, causing the left motor to travel in reverse. Spikes in the speed data in the negative direction show periods of slippage where the ballast gave way under torque, causing the motor to spin up as traction was lost. Saturation of the current at the maximum allowed value of 50 A can be seen frequently, demonstrating the high torque nature of this maneuver, and periods of simultaneous current saturation and zero motor speed demonstrate how power can be insufficient when ample traction is available. Additionally, periods of forward motion show moments where the position of the TCR was adjusted to attempt turning at a different location, and a longer period of forward motion around 65 s shows where the TCR was repositioned a short distance down the track midway through the turn to attempt the second half in a different location. The issue with traction is fundamental to the operating conditions, as the ballast will slip easily during high torque maneuvers. However, there is potential that the insufficient power issue could be mitigated. Increasing the maximum allowed current will increase

torque [45], and the limiting factor for maximum continuous current is the ESC itself, which recommends a maximum value of 50 A while the motors are capable of 80 A each. This maximum current could potentially be increased if it can be shown that operation at a higher value does not cause overheating within the ESC. The ESCs' operating conditions, being exposed to ambient air and mounted onto a moving platform, create the potential for effective convective heat transfer, allowing for operation at higher current values. Future work could include temperature data collection at currents higher than 50 A in normal operating conditions to investigate the thermal response and determine if more power can be safely applied.

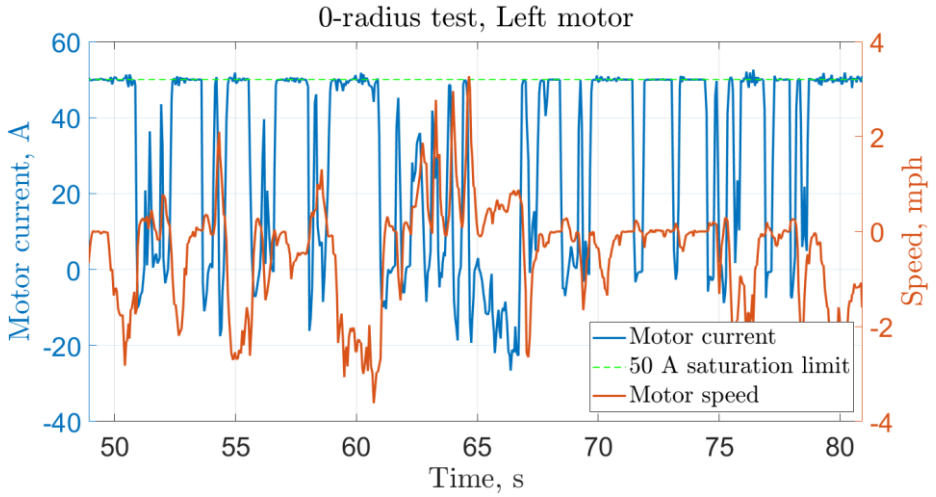

Figure 29. Current and speed data collected from the left motor during the 0−radius test showed periods of stalling and spikes in speed, indicating slippage.

Rail climbing was intermittent when climbing into the track bed and was unsuccessful when attempting to climb out. The TCR had enough torque to pull itself up over the rail; however, the railhead would contact the leading edge of a protective plate located on the undercarriage of the TCR used to protect electronics from impact, causing the TCR to stop in place. The edge of this plate could be cleared at times, but the railhead would then rest on it, reducing the load on the tracks, reducing traction, and causing the tracks to slip across the surface of the railhead. These issues caused rail climbing to be intermittent, and when combined with the traction difficulties inherent to the track bed, it was unsuccessful when attempting to climb out. For rail climbing to be consistent and successful, modifications such as the addition of more sets of undercarriage idlers should be investigated to attempt to prevent interference from the protective plate and ensure that the tracks bear the full weight of the TCR throughout the maneuver. Additionally, weights at the front of the TCR could be used to shift the center of gravity forward and cause the TCR to tip over the rail at an earlier location. A video has been included showing the mobility test.

The footage from the constant speed tests shows that the TCR traverses smoothly over the ties at 1.6 km/h while the front was occasionally knocked slightly airborne during the 3.2 km/h test; however, the TCR was consistently and violently knocked airborne during the 4.8 km/h test, Figure 30. The conditions in the track bed appear slightly rougher than those in the Test Bed, as significant collisions were not observed until 6.8 km/h over the Test Bed. With the TCR's rigid construction, these collisions impart large shock loads to the TCR, which could be detrimental to its reliability over time. The TCR remains uncontrollable while it is airborne.

Lastly, after the tests were completed, the TCR was driven across the track bed, and the left track came apart without warning. Inspection showed a critically bent pin caused the failure, and multiple other pins were plastically deformed. It is unclear whether these failures are due to the age of the tracks (being a few years old) or simply the significant shock loads during high-speed tests. It is concluded, however, that unless means for managing the shock loads inherent to traversing at speeds greater than 3.2 km/h are implemented into the TCR's design, its speed should be limited to 3.2 km/h for track bed operations. A video has been included showing one of the constant speed tests at 3.2 km/h. The TCR becomes much less controllable and prone to component failure above this speed, although the inclusion of suspension or other systems aiding in increasing controllability and reliability could be investigated in the future to further increase the system's efficiency. At this speed, the TCR will travel the length of a typical railcar (18 m) in 20 s, much quicker than the manual inspections. Therefore, even limited to this speed, it would be possible for the TCR to traverse the entire train length, labeling potential defects for further investigation by the following carmen if autonomous control and defect detection are realized.

Figure 30. Track bed testing results compare the impacts experienced at 3.2 km/h (**left**) and 4.8 km/h (**right**).

Therefore, the TCR is capable of intermittently climbing into the track bed, turning within the track bed, traversing at speeds greater than manual inspections, and is not yet able to climb out. Although imperfect, the TCR is in a category of its own as a self-propelled robot for undercarriage inspection in the railyard and siding environments. Further work is underway to correct these mobility shortcomings, and the authors are confident that the TCR will soon be capable of completing these inspections without any manual assistance, a capability that is not possible for any other systems, to the knowledge of the authors. The closest analogy is the robot developed by Chiaradia et al. [34] This robot could operate in the railyard and siding environments provided the rail is continuous and not jointed; however, it needs to be manually installed and uninstalled between the rails.

5.4. PID Control System Validation

The system's step response during the 3.2 km/h test, Figure 31, shows the system's ability to respond to a step input quickly and maintain a testing speed averaged around the input value. However, the high-disturbance track bed environment prevents the response from ever truly settling. Collisions and resistance changes cause the TCR to decelerate rapidly. As the control system increases motor power in response, sudden drops in resistance can then lead to overshoot. The integral term in the PID system ensures that the speed will average to a value very close to what has been commanded, but currently, speed variations can be expected throughout the test. Significant improvements to the steady-state response of the system would most likely require improvements to the dynamics of the TCR. Methods for dampening the disturbances from the track bed environment, such as suspension, could be investigated as means for improving this response. The 10–90% rise time of the system is 0.3 s, indicating an excellent ability to quickly reach testing speeds.

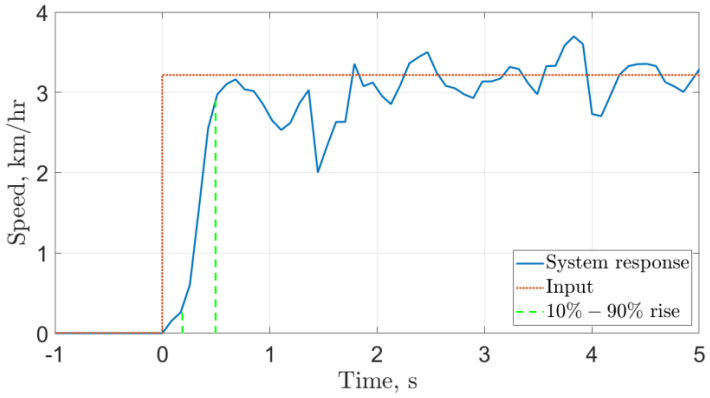

Figure 31. Step response during the 3.2 km/h test within the track bed.

5.5. FPV System Validation

Feedback from the FPV system was used to control the TCR on the Test Bed without contacting the sides of the bed at speeds up to 4.8 km/h, Figure 32a. This test qualitatively demonstrates that the FPV system operates with low enough latency to be sufficient for feedback even when large disturbances are present. Additionally, it shows that high vibrations do not degrade imaging performance to the point of becoming uncontrollable.

Tests conducted up to 9.6 km/h beneath the trailer indicate the FPV system's ability to operate in similar lighting conditions as seen beneath the railcars. The FPV camera effectively altered its sensitivity to provide a clear image while both beneath the trailer and the sky; although, as expected, periods of saturation or dimness occurred when transitioning from dim to bright (Figure 32b) and vice versa, respectively. However, the length of these transitions was relatively short, and the TCR was still able to be controlled at twice the speed that will be seen in the track bed, effectively showing that lighting conditions will not significantly hinder controllability beneath the railcar and that the latency inherent to the system is sufficiently low not to be a limiting factor. Therefore, the FPV system is adequate for supplying an operator with constant feedback sufficient for control of the TCR in the track bed.

(**a**) (**b**)

Figure 32. FPV testing results: (**a**) 4.8 km/h test over Test Bed showing the ability to operate in high vibratory conditions; (**b**) 9.6 km/h under the trailer showing a dark to light transition.

6. Conclusions

The results presented in this paper demonstrate an array of distinct improvements to the design and operations of the TCR, including:

- Improvement of the effective FOV from 30% of the required value to over 100%

- Elimination of motion blur
- Adequate lighting across the entire FOV
- Implementation of PID control
- Inclusion of a real-time video feed for operator feedback
- Improvements to the reliability of the track bed environment

Future work must address the intermittent rail climbing. To successfully complete the inspection, the TCR must be able to position itself within the rails unassisted. Longer tests should be completed at 3.2 km/h to verify the system's reliability at this operating speed. Lastly, images should also be gathered from rolling stock to investigate if any unforeseen issues arise in the working environment.

Together, these improvements have equipped the TCR to traverse the track bed at speeds three times greater than manual inspections while gathering clear, well-lit images of entire rolling stock undercarriages. Combined with the control improvements, the TCR could be used to provide a supplementary view for carmen during stationary inspections on revenue service tracks, bringing WTMS-level technology to railyards on a mobile, cost-effective platform. Additionally, these images could be incorporated into an AI or ML image processing model for autonomous defect detection, allowing the carmen to focus their efforts on the components of the rolling stock suspected of containing defects. Autonomous control could also be examined for the TCR while operating within the track bed to allow the carmen to focus on the inspection fully. As shown, the TCR's capabilities have been greatly expanded through the work presented, and the system is now capable of performing tasks unique to this platform. Future work should focus on the remaining mobility and reliability concerns raised by this study and may also investigate the inclusion of automated models for defect detection.

Supplementary Materials: The following supporting information can be downloaded at: https://zenodo.org/records/12740906?token=eyJhbGciOiJIUzUxMiJ9.eyJpZCI6ImZlYzg4ODgyLTQ2YmQtNDA0YS1hNGUxLTdhOTE2NzUwMWRjMCIsImRhdGEiOnt9LCJyYW5kb20iOiI2NTZjZDAwZmM2YjhkYjQ4OTgxNmRkOTRkMzc4MzY1OSJ9.kRFd34KYzxG5QynTNSsu6ckPW8wEMQgyMUgorm9agXm9PMzexj1vQ-plgwYSrXDonCZfV5be2A4sEYkusZ54aw, accessed on 20 April 2024. Video S1. Under-train operation. Video S2. Poster test with automatic shutter speed. Video S3. Poster test with 1/960 s. shutter speed. Video S4. Poster test with 1/1920 s. shutter speed. Videos S5–S7. Under-truck tests with original lighting (vertical, right, and left views). Videos S8–S10. Under-truck tests with improved lighting using wax paper and plexiglass diffusive coverings (vertical, right, and left views). Videos S11–S13. Under-trailer test (vertical, right, and left views). Video S14. Mobility test from local tracks showing intermittent rail climbing in, turning within the rails, and an inability to climb back out. Video S15. 3.2 km/h tests at the local tracks.

Author Contributions: Design assessment, J.K.; redesign and modification, J.K.; testing, J.K.; analysis, J.K.; data curation, J.K.; writing, J.K.; review and editing, J.K. and M.A.; supervision, M.A.; project administration, M.A.; funding acquisition, M.A. All authors have read and agreed to the published version of the manuscript.

Funding: This research was funded by the US Department of Transportation grant number 69A3551747132.

Data Availability Statement: The original contributions presented in the study are included in the article/Supplementary Material, further inquiries can be directed to the corresponding author.

Conflicts of Interest: The authors declare no conflicts of interest.

References and Notes

1. Freight Rail Overview. FRA. 2020. Available online: https://railroads.dot.gov/rail-network-development/freight-rail-overview (accessed on 22 April 2024).
2. Train Accidents and Rates. FRA. Available online: https://safetydata.fra.dot.gov/OfficeofSafety/publicsite/Query/TrainAccidentsFYCYWithRates.aspx (accessed on 22 April 2024).
3. Austin, K.B. Hotbox Signal for Railway Trains. U.S. Patent 2486546, 1 November 1949.
4. Tarawneh, C.; Aranda, J.; Hernandez, V.; Crown, S.; Montalvo, J. An Investigation into Wayside Hot-Box Detector Efficacy and Optimization. *Int. J. Rail Transp.* **2020**, *8*, 264–284. [CrossRef]

5. Post, W.M. Protective System for Railways. U.S. Patent 2095616, 12 October 1937.
6. Fu, W.; He, Q.; Feng, Q.; Li, J.; Zheng, F.; Zhang, B. Recent Advances in Wayside Railway Wheel Flat Detection Techniques: A Review. *Sensors* **2023**, *23*, 3916. [CrossRef] [PubMed]
7. Stratman, B.; Liu, Y.; Mahadevan, S. Structural Health Monitoring of Railroad Wheels Using Wheel Impact Load Detectors. *J. Fail. Anal. Prev.* **2007**, *7*, 218–225. [CrossRef]
8. Bi, L.; Zhao, P.; Teng, M.; Zhao, L.; Liu, X.; Xing, M. Wayside Testing Methods for High-Frequency Vertical Wheel-Rail Impact Forces and Its Applicability. *Measurement* **2020**, *151*, 107197. [CrossRef]
9. Silva, R.; Guedes, A.; Ribeiro, D.; Vale, C.; Meixedo, A.; Mosleh, A.; Montenegro, P. Early Identification of Unbalanced Freight Traffic Loads Based on Wayside Monitoring and Artificial Intelligence. *Sensors* **2023**, *23*, 1544. [CrossRef] [PubMed]
10. Cortis, D.; Bruner, M.; Malavasi, G. Development of a Wayside Measurement System for the Evaluation of Wheel-Rail Lateral Contact Force. *Measurement* **2020**, *159*, 107786. [CrossRef]
11. Giannouli, E.; Papaelias, M.; Amini, A.; Huang, Z.; Jantara, V.L.; Kerkyras, S.; Krusuansombat, P.; Garcia Marquez, F.P.; Vallely, P. Detection and Evaluation of Rolling Stock Wheelset Defects Using Acoustic Emission. *Insight Non Destr. Test. Cond. Monit.* **2021**, *63*, 403–408. [CrossRef]
12. Hart, J.M.; Resendiz, E.; Freid, B.; Sawadisavi, S.; Barkan, C.P.L.; Ahuja, N. Machine Vision Using Multi-Spectral Imaging for Undercarriage Inspection of Railroad Equipment. In Proceedings of the 8th World Congress on Railway Research, Seoul, Republic of Korea, 18–22 May 2008.
13. Schlake, B.W.; Edwards, J.R.; Hart, J.M.; Barkan, C.P.L.; Todorovic, S.; Ahuja, N. Automated Inspection of Railcar Underbody Structural Components Using Machine Vision Technology 09-2863. In Proceedings of the Transportation Research Board 88th Annual Meeting, Washington, DC, USA, 11–15 January 2009.
14. Freid, B.; Barkan, C.P.L.; Ahuja, N.; Hart, J.M.; Todorvic, S.; Kocher, N. Multispectral Machine Vision for Improved Undercarriage Inspection of Railroad Rolling Stock. In Proceedings of the International Heavy Haul Conference, Kiruna, Sweden, 11–13 June 2007; pp. 737–744.
15. Thillaikkarasi, R.; Yaseen, M.M.; Rameshbabu, R.; Prabhakaran, R.; Kesavan, R.; Jose Anand, A. Waysides Inspection Using Wayside Processing Imaging and Deep Learning. In Proceedings of the 2023 3rd International Conference on Pervasive Computing and Social Networking, ICPCSN 2023, Salem, India, 19–20 June 2023; Institute of Electrical and Electronics Engineers Inc.: Piscataway, NJ, USA, 2023; pp. 359–365. [CrossRef]
16. Raghava Prasad, C.; Kishore, P.V.V. Performance of Active Contour Models in Train Rolling Stock Part Segmentation on High-Speed Video Data. *Cogent. Eng.* **2017**, *4*, 1279367. [CrossRef]
17. Norfolk Southern Corporation. Norfolk Southern Launches AI Train Inspection Technology. PR Newswire. 2023. Available online: https://www.prnewswire.com/news-releases/norfolk-southern-launches-ai-train-inspection-technology-301968329.html (accessed on 22 April 2024).
18. Nayebi, K. Vision System Tracks Trouble with Trains. Vision Systems. 2012. Available online: https://www.vision-systems.com/non-factory/security-surveillance-transportation/article/16737816/vision-system-tracks-trouble-with-trains (accessed on 22 April 2024).
19. Gratas, S. Jackson Rail Line Gets Latest Tech in Norfolk Southern's Efforts to Improve Safety. GPB. 2024. Available online: https://www.gpb.org/news/2024/04/12/jackson-rail-line-gets-latest-tech-in-norfolk-southerns-efforts-improve-safety (accessed on 22 April 2024).
20. Pre-Departure Inspection. Title 49 U.S. Code of Federal Regulations § 215.13. 1980.
21. Freight Rail & Train Length. Association of American Railroads. Available online: https://www.aar.org/issue/freight-train-length/#:~:text=In%202023,%20the%20median%20length,were%20longer%20than%2014,000%20feet (accessed on 22 April 2024).
22. Maratea, A.; Grissom, D. The East Palestine Derailment & Overall Rail Industry Safety. Transportation Communications Union. Available online: https://www.tcunion.org/tcu-union/the-east-palestine-derailment-overall-rail-industry-safety/ (accessed on 22 April 2024).
23. Schlake, B.W.; Barkan, C.P.L.; Edwards, J.R.; Riley Edwards, J. Impact of Automated Condition Monitoring Technologies on Railroad Terminal Performance. In Proceedings of the 2010 Annual AREMA Conference, Orlando, FL, USA, 29 August−1 September 2010.
24. Schoenherr, E.; Smuda, B. Under-Vehicle Autonomous Inspection through Undercarriage Signatures. In *Unmanned Ground Vehicle Technology VII*; SPIE: Bellingham, WA, USA, 2005; p. 645. [CrossRef]
25. Our Products. Techmatics NZ. Available online: https://techmatics.co.nz/our-products/ (accessed on 22 April 2024).
26. Jing, G.; Qin, X.; Wang, H.; Deng, C. Developments, Challenges, and Perspectives of Railway Inspection Robots. *Autom. Constr.* **2022**, *138*, 104242. [CrossRef]
27. Railway Inspection Robot. Shenhao Robotics. Available online: https://www.shenhaorobotics.com/railway-inspection-robot/ (accessed on 21 April 2024).
28. Railway. Loccioni. Available online: https://www.loccioni.com/en/railway/ (accessed on 21 April 2024).
29. Daniyan, I.; Mpofu, K.; Nwankwo, S. Design of a Robot for Inspection and Diagnostic Operations of Rail Track Facilities. *Int. J. Qual. Reliab. Manag.* **2023**, *40*, 653–673. [CrossRef]
30. ANYbotics and Stadler Service AG Explore the Future of Train Maintenance. ANYbiotics. 2021. Available online: https://www.anybotics.com/news/robotic-inspection-in-train-maintenance/ (accessed on 22 April 2024).

31. Kiselev, G.G.; Korkina, S.V. Automation of Inspection of Rolling Stock at a Maintenance Point Using a Robotic Complex. In *AIP Conference Proceedings*; AIP Publishing: Melville, NY, USA, 2023. [CrossRef]
32. Yue, S.; Haishan, Z.; Hao, Y.; Zhen, J.; Shen Tao, J. Research and Design of a Multi Track Daily Inspection Robot for Urban Rail Transit. In Proceedings of the 14th International Conference on Measuring Technology and Mechatronics Automation, Changsha, China, 15–16 January 2022; Institute of Electrical and Electronics Engineers Inc.: Piscateville, NJ, USA, 2022; pp. 528–531. [CrossRef]
33. Zhang, M.; Ma, L.; Shen, K.; Sun, Y. Autonomous Localization and Motion Control of Under-Vehicle Inspection Robot. In *IFAC-PapersOnLine*; Elsevier: Amsterdam, The Netherlands, 2023; pp. 3060–3065. [CrossRef]
34. Chiaradia, D.; Leonardis, D.; Manno, V.; Solazzi, M.; Masini, P.; Frisoli, A. A Mobile Robot for Undercarriage Inspection on Standard Railway Tracks. In *Advances in Italian Mechanism Science (Proceedings of the 3rd International Conference of IFToMM Italy)*; Springer: Berlin/Heidelberg, Germany, 2021; pp. 362–369.
35. Molzon, M.; Ahmadian, M. Development of a Mobile Robot System for the Visual Inspection of Railcar Undercarriage Equipment. In Proceedings of the 2022 Joint Rail Conference, Online, 20–21 April 2022.
36. 4750 Cu. Ft. Covered Hopper. BNSF Railway. Available online: https://www.bnsf.com/ship-with-bnsf/ways-of-shipping/equipment/pdf/Large.pdf (accessed on 22 April 2024).
37. 136-Lb/Yd AREMA Rail. Harmer Steel. 2010. Available online: https://www.harmersteel.com/tee-rails/136-lb-yd-arema-rail/ (accessed on 22 April 2024).
38. Electric Skateboard Motor 6355 190 KV. Torque Boards. Available online: https://diyelectricskateboard.com/products/electric-skateboard-motor-6355-190kv (accessed on 15 June 2024).
39. What Is Gear Ratio & How Do You Calculate It? Accu. Available online: https://accu-components.com/us/p/442-what-is-gear-ratio (accessed on 15 June 2024).
40. ANSI Standard Rolling Chain. Renold Jeffrey. Available online: https://www.renoldjeffrey.com/media/2395574/ansi-standard-roller-chain-renold-jeffrey.pdf (accessed on 15 June 2024).
41. 6105 Aluminum Extrusions. Tri-State Aluminum. Available online: https://tri-stateal.com/aluminum-alloy-6105/#:~:text=6105%20aluminum%20and%206061%20aluminum,is%20less%20sensitive%20to%20quenching (accessed on 15 June 2024).
42. Von Mises Criterion (Maximum Distortion Energy Criterion). Engineers Edge. Available online: https://www.engineersedge.com/material_science/von_mises.htm (accessed on 15 June 2024).
43. Fastener Bolt Thread Stress Tensile Area Table Chart for ANSI Inch Size. Engineers Edge. Available online: https://www.engineersedge.com/fastener_thread_stress_area.htm (accessed on 22 April 2024).
44. FPV Camera Latency Testing. Oscar Liang. 2021. Available online: https://oscarliang.com/fpv-camera-latency/ (accessed on 22 April 2024).
45. Tang, J. Technical Manual Series: Brushless Motor Drive Systems and Motor Torque. Oriental Motor. 2021. Available online: https://blog.orientalmotor.com/technical-manual-series-brushless-motor-drive-systems-and-motor-torque (accessed on 22 April 2024).